iScience

CellPress
OPEN ACCESS

Article

RNA molecules display distinctive organization at nuclear speckles

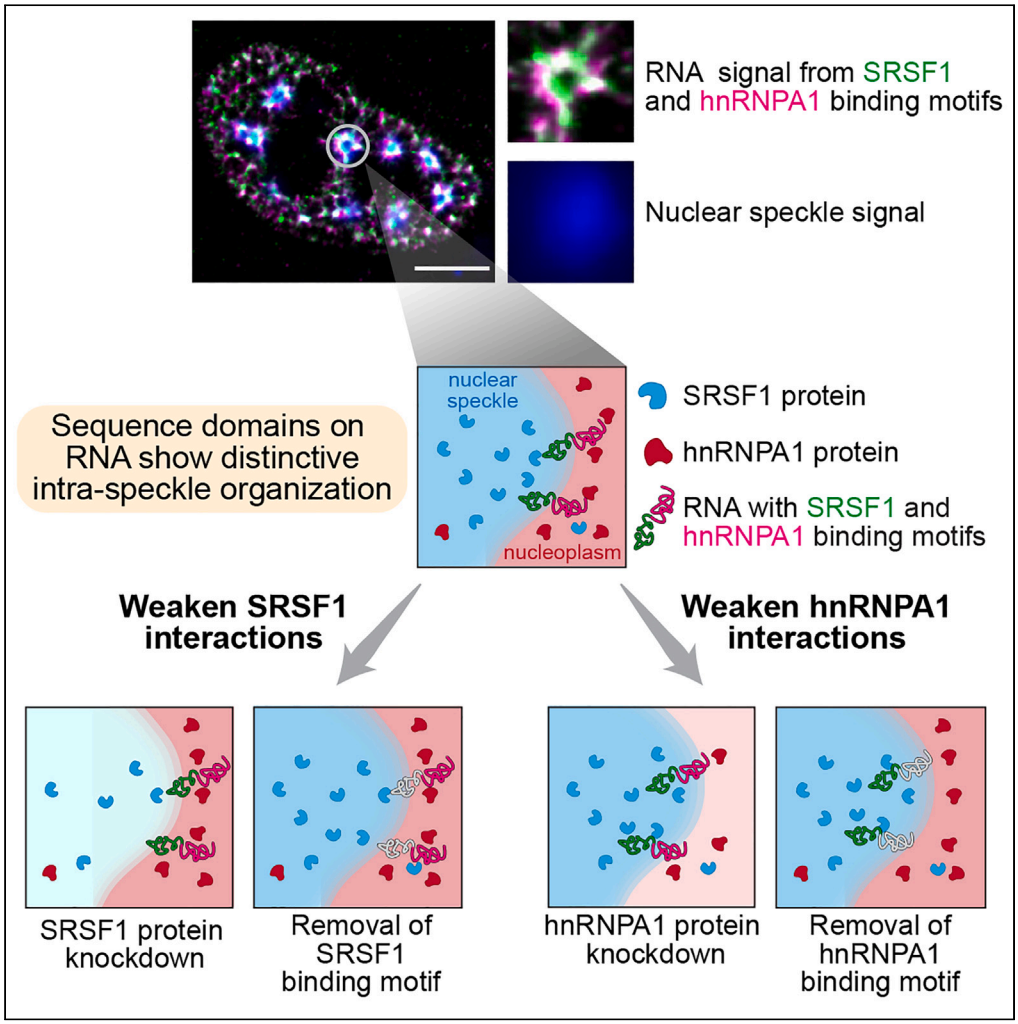

Sneha Paul, Mauricio A. Arias, Li Wen, ..., Xiaoshu Wang, Oded Regev, Jingyi Fei

regev@cims.nyu.edu (O.R.)
jingyifei@uchicago.edu (J.F.)

Highlights

Regions in RNA exhibit distinct positioning and orientation at nuclear speckles

SR motif-enriched regions localize closer to speckle center than hnRNP ones

RNA organization is driven by interactions with proteins inside and outside speckle

Paul et al., iScience 27, 109603
May 17, 2024
https://doi.org/10.1016/j.isci.2024.109603

iScience

CellPress
OPEN ACCESS

Article

RNA molecules display distinctive organization at nuclear speckles

Sneha Paul,[1,8,10] Mauricio A. Arias,[2,3,10] Li Wen,[4,11] Susan E. Liao,[2,11] Jiacheng Zhang,[5,9] Xiaoshu Wang,[6] Oded Regev,[2,*] and Jingyi Fei[1,7,12,*]

SUMMARY

RNA molecules often play critical roles in assisting the formation of membraneless organelles in eukaryotic cells. Yet, little is known about the organization of RNAs within membraneless organelles. Here, using super-resolution imaging and nuclear speckles as a model system, we demonstrate that different sequence domains of RNA transcripts exhibit differential spatial distributions within speckles. Specifically, we image transcripts containing a region enriched in binding motifs of serine/arginine-rich (SR) proteins and another region enriched in binding motifs of heterogeneous nuclear ribonucleoproteins (hnRNPs). We show that these transcripts localize to the outer shell of speckles, with the SR motif-rich region localizing closer to the speckle center relative to the hnRNP motif-rich region. Further, we identify that this intra-speckle RNA organization is driven by the strength of RNA-protein interactions inside and outside speckles. Our results hint at novel functional roles of nuclear speckles and likely other membraneless organelles in organizing RNA substrates for biochemical reactions.

INTRODUCTION

Eukaryotic cells contain many membraneless organelles with distinct nuclear[1,2] or cytoplasmic localizations.[3,4] These membraneless organelles generally contain RNAs, RNA binding proteins (RBPs), and ribonucleoprotein (RNP) assemblies.[5,6] Multivalent interactions between protein and RNA components drive the formation of these organelles through phase separation,[7–11] and can also lead to the formation of subdomains or layered structures within many of them.[12]

Little is known about the organization of RNA within membraneless organelles, despite its potential role in coordinating biochemical reactions. One exception is the 22 kb long noncoding RNA (lncRNA) *NEAT1*, which serves as a scaffold component of paraspeckles and is organized with its 5′- and 3′- ends at the paraspeckle shell and its central region at the paraspeckle core.[13] However, most RNAs are not considered scaffold components. For such non-scaffold, or client RNA transcripts, different localizations of transcripts around or within some membraneless organelles (such as germ granules, nuclear speckles, and stress granules) have been noted.[14–16] These studies, however, report the localization of RNA transcripts as one entity; whether there is any organization at the level of individual molecules, i.e., between different sequence domains of the same client RNA, is not clear. Another shortcoming of most previous work is the lack of mechanistic insight explaining the observed localization.

We reasoned that the differential proteome composition inside and outside of a membraneless organelle can lead to a distinctive organization of RNA molecules. Specifically, regions of RNA transcripts interacting with proteins inside the organelle will tend to localize closer to the center than regions interacting with proteins outside the organelle. In this way, the position of RNA transcripts will be driven to the outer shell of the membraneless organelle, and their orientation will be constrained (Figure 1). Here, we refer to the position and orientation of RNA transcripts collectively as intra-organelle RNA organization.

We sought to test this intra-organelle RNA organization model using nuclear speckles as a model system. Nuclear speckles are a type of membraneless organelle in higher eukaryotic cells, playing important roles in regulating transcription, splicing, and RNA processing.[17–20] Their number ranges between 20 and 50 per cell,[21] and their size varies from a few hundred nanometers to a few microns.[21] Nuclear speckles

[1]Department of Biochemistry and Molecular Biology, The University of Chicago, Chicago, IL 60637, USA
[2]Courant Institute of Mathematical Sciences, New York University, New York, NY 10012, USA
[3]Institute for System Genetics, NYU Langone Health, New York, NY 10016, USA
[4]Department of Physics, The University of Chicago, Chicago, IL 60637, USA
[5]Graduate Program in Biophysical Sciences, The University of Chicago, Chicago, IL 60637, USA
[6]The College, The University of Chicago, Chicago, IL 60637, USA
[7]Institute for Biophysical Dynamics, The University of Chicago, Chicago, IL 60637, USA
[8]Present address: CNRS-Institute of Molecular Sciences of Orsay, Paris-Saclay University, 91405 Orsay, France
[9]Present address: ReviR Therapeutics, Shenzhen 518000, China
[10]These authors contributed equally
[11]These authors contributed equally
[12]Lead contact
*Correspondence: regev@cims.nyu.edu (O.R.), jingyifei@uchicago.edu (J.F.)
https://doi.org/10.1016/j.isci.2024.109603

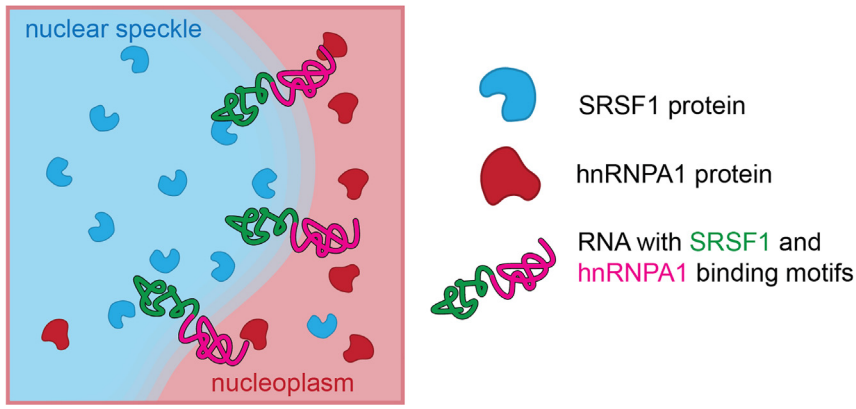

Figure 1. Intra-organelle RNA organization model with nuclear speckle as an example

Nuclear proteins show differential localization with respect to nuclear speckles, with SRSF1 protein enriched in speckles and hnRNPA1 protein distributed in the nucleoplasm and slightly depleted in the speckle. As a result, RNAs containing both RBP-binding motifs will be driven to the outer shell of nuclear speckles and will be organized with their SRSF1-binding motifs closer to the speckle center than their hnRNPA1-binding motifs. Also see Figure S1.

are rich in small nuclear RNAs (snRNAs), spliceosomal proteins, and certain splicing factors, including SR proteins (a family of RBPs named for containing regions with repetitive serine and arginine residues). Polyadenylated RNAs, stained with fluorescently labeled polyT oligos, are observed to localize to nuclear speckle.[22,23] Moreover, a recent transcriptomic analysis has systematically identified nuclear speckle-localized transcripts.[24] Nuclear speckles exhibit a core-shell organization. Specifically, the scaffold proteins SON and SRRM2 form the core layer of speckles, while spliceosomal components, including snRNAs and spliceosomal proteins as well as the nuclear speckle-localized lncRNA *MALAT1*, are enriched in the outer shell.[16] In contrast to paraspeckles, nuclear speckles are not known to depend on any specific RNA transcript for their formation.

Nuclear speckles are well suited as a model system for two reasons. First, proteins with different localization relative to nuclear speckles were previously noted. Specifically, certain SR proteins are enriched in nuclear speckles,[25,26] whereas certain heterogeneous nuclear ribonucleoproteins (hnRNPs) do not exhibit any enrichment or might be depleted from speckles.[27,28] Second, synthetic reporter constructs can be designed to generate nuclear speckle-localized RNA transcripts.[29]

In this work, we use super-resolution microscopy to demonstrate that the intra-organelle RNA organization model applies to nuclear speckles (Figure 1). Our data illustrate that different sequence domains within an RNA transcript exhibit differential spatial distributions within speckles, a phenomenon driven by RNA-protein interactions within and outside nuclear speckles. Our results suggest potential functional roles of membraneless organelles in coordinating biochemical reactions through organizing RNA substrates.

RESULTS

SRSF1 and hnRNPA1 proteins exhibit distinct localization relative to nuclear speckles

Confirming previous results, we found that SRSF1 protein was consistently enriched in nuclear speckles[24,25,30] (Figure S1A), whereas hnRNPA1 proteins showed a lower abundance in most nuclear speckles than the surrounding nucleoplasm[31] (Figure S1B). In summary, SRSF1 and hnRNPA1 concentrations inside nuclear speckles are distinct from those outside (Figure S1C), justifying the choice of this SR-hnRNP protein pair for further analysis.

Transcripts containing SRSF1- and hnRNPA1-binding motifs localize to nuclear speckles

We started by synthesizing a reporter construct ($WT_{S1\text{-}H1}$) using the Tet-responsive promoter-controlled three-exon design based on the Chinese hamster *DHFR* gene from our earlier work.[32] Previous studies indicate that genomic exonic regions are more frequently enriched in SRSF1-binding motifs while intronic regions are more enriched in hnRNPA1-binding motifs.[33,34] Therefore, we included multiple SRSF1-binding motifs in the middle exon and multiple hnRNPA1-binding motifs in the downstream intron (Figure 2A). We verified using BLAST (Basic Local Alignment Search Tool) that these sequences exhibit minimal homology with endogenous sequences. The construct was transfected into a HeLa cell line with stably expressed Tet-regulated transactivator Tet-On 3G, and RNA expression was induced with doxycycline for either 30 min or 2 h. Using a reverse-transcription polymerase chain reaction (RT-PCR) assay, we validated that $WT_{S1\text{-}H1}$ underwent normal splicing (Figure S2A).

Localization of $WT_{S1\text{-}H1}$ transcripts was first examined using diffraction-limited fluorescence microscope. Using fluorescence *in situ* hybridization (FISH), we labeled the SRSF1- and hnRNPA1-binding motifs on the RNA transcripts with CF568 and Alexa Fluor 647 (AF647), respectively (Figure S3). Nuclear speckles were stained with Alexa Fluor 488 (AF488)-labeled antibody against the scaffold protein SRRM2.[35] Minimal non-specific binding of the RNA FISH probes was detected using cells with unsuccessful transfection as controls (Figure S3B). In addition, transfection and expression of the construct did not change the localization of SRSF1 or hnRNPA1 proteins relative to nuclear speckles (Figure S1C). At 30 min induction, the colocalized FISH signals from both SRSF1 and hnRNPA1 motifs from the $WT_{S1\text{-}H1}$ construct appeared as

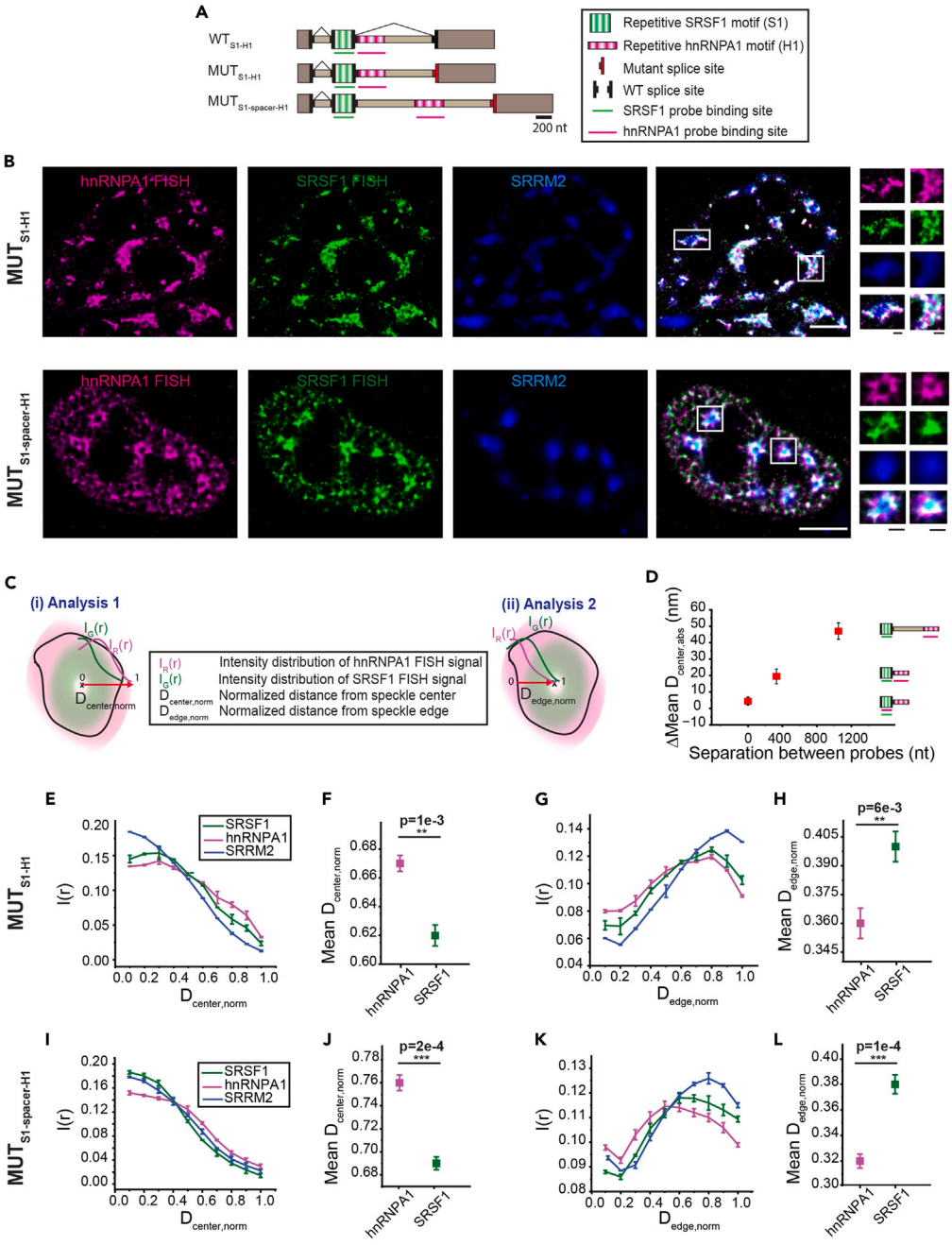

Figure 2. SMLM imaging and analysis of intra-speckle organization of RNAs containing SRSF1 motifs in exon and hnRNPA1 motifs in intron

(A) Schematic illustration of $WT_{S1\text{-}H1}$, $MUT_{S1\text{-}H1}$ and $MUT_{S1\text{-}spacer\text{-}H1}$ constructs.

(B) Representative SMLM image of $MUT_{S1\text{-}H1}$ and $MUT_{S1\text{-}spacer\text{-}H1}$. FISH signals corresponding to hnRNPA1 (labeled with AF647) and SRSF1 (labeled with CF568) motifs in the RNAs are shown in magenta and green, respectively. Immunostaining of SRRM2 is shown in blue. Scale bar represents 5 μm (white) and 1 μm (black).

(C) Calculation of the distribution of FISH signal as a function of the distance from the center of the nuclear speckle (i) and edge of the nuclear speckle (ii). Due to size differences among nuclear speckles, distances are all normalized from the center of the speckle (i) or the edge of the speckle (ii) to build the overlaid distribution. The black line represents the nuclear speckle edge; the pink and green lines are the intensity distributions of the RNA FISH signals of the hnRNPA1 and SRSF1 motifs. The speckle edge was determined using a MATLAB built-in function *bwboundaries* which identifies the pixels at the edge of the intensity mask of each speckle.

(D) Plot of difference in absolute mean distance vs. separation in the RNA length (in the unit of nucleotide) between the probe targeting positions.

(E and G) Population distribution of SRSF1 and hnRNPA1 motif signals for $MUT_{S1\text{-}H1}$ as a function of the normalized distance from the center of the speckle (E) and edge of the speckle (G).

Figure 2. *Continued*

(F and H) Population-weighted mean normalized distance of SRSF1 and hnRNPA1 signal from the center of speckle (F) and edge of speckle (H) for each speckle for $MUT_{S1\text{-}H1}$.

(I and K) Population distribution of SRSF1 and hnRNPA1 motif signals for $MUT_{S1\text{-}spacer\text{-}H1}$ as a function of the normalized distance from the center of the speckle (I) and edge of the speckle (K).

(J and L) Population-weighted mean normalized distance of SRSF1 and hnRNPA1 signal from the center of speckle (J) and edge of speckle (L) for each speckle for $MUT_{S1\text{-}spacer\text{-}H1}$. Error bars in the population vs. distance plots report the standard deviation (n = 2) from two replicates, each replicate containing at least 60–90 nuclear speckles collected from 4 to 6 cells. Scatterplots are generated by combining all nuclear speckles (120–180) from two replicates. Values in scatterplot represent mean ± standard error of mean (SEM). *p* values in the scatterplots are calculated with paired sample Wilcoxon signed rank test (one-sided), with $*p < 5e\text{-}2$, $**p < 1e\text{-}2$, $***p < 1e\text{-}3$. Replicates are biological replicates collected starting from different dishes of cells and measured on different days. Also see Figures S4–S6 and S10.

bright foci and were mostly localized to nuclear speckles (Figure S3C). At 2 h induction, a significant portion of the FISH signal for the SRSF1 motifs was localized to the cytoplasm, corresponding to the spliced and exported mRNAs, whereas the residual nuclear-localized signals from the SRSF1 and hnRNPA1 motifs remained localized to nuclear speckles, likely corresponding to the remaining pre-mRNA transcripts accumulated at transcription sites (Figure S3C). This result implies that $WT_{S1\text{-}H1}$ could mimic certain speckle-associated endogenous genes, whose transcripts localize to speckle before nuclear export.

Transcripts containing SRSF1- and hnRNPA1-binding motifs display distinctive intra-speckle organization

We next sought to determine the organization of RNA in nuclear speckles. One challenge is to ensure that we are imaging RNA transcripts containing both SRSF1 and hnRNPA1 motifs, rather than spliced products or intron lariats. In the case of $WT_{S1\text{-}H1}$, while the colocalized CF568 and AF647 foci are likely to mainly consist of pre-mRNAs, spliced products and intron lariats carrying CF568 and AF647 signals, respectively, may also localize to the same foci. Signals coming from separated RNA molecules can complicate interpretation of the imaging results. We therefore synthesized a reporter construct $MUT_{S1\text{-}H1}$ with a mutation at the 3′ splice site of the second intron (AG>GG) which inhibits its splicing (Figure 2A).[36,37] Using an RT-PCR assay, we verified that the second intron of $MUT_{S1\text{-}H1}$ RNA was mostly unspliced (Figure S2B), thereby leaving the SRSF1- and hnRNPA1-binding motifs on the same RNA molecule. Moreover, epifluorescence imaging confirmed that $MUT_{S1\text{-}H1}$ RNAs are localized in nuclear speckles (Figure S3A).

A second challenge is the small distance expected between the SR and hnRNP motifs. Indeed, since both are on the same RNA transcript with the centers of the two regions separated by only ~400 nt, we expect a distance not greater than 50 nm (e.g., the typical physical size of a regular-sized RNA molecule [hundreds to a few thousand nucleotides] is ~40–100 nm, as characterized in solution and in fixed cells[38–41]). We therefore performed super-resolution imaging using single-molecule localization microscopy (SMLM), with a spatial resolution of 10–30 nm.[42] An epifluorescence image of SRRM2 was recorded to locate the speckles and adjust the focal plane to be through the middle of most of the speckles, and 2D-SMLM imaging was performed on the same cell.

As expected, even with the increased resolution, the resulting images showed rather subtle differences between the two FISH signals at the level of individual speckles (Figure 2B). To obtain statistically significant results, we therefore developed a data analysis pipeline (Figure S4) that averages the results across a population of nuclear speckles (~50–90 per replicate). Specifically, we first selected nuclear speckles containing associated RNA signals by using intensity thresholding on the sum of all three channels, namely the two RNA FISH signal channels and the nuclear speckle marker channel (Figure S4, (1)). Extremely small, large, and irregular nuclear speckles were excluded from the analysis through size and ellipticity cutoffs (Figure S4, (2)). The radial signal intensity distributions from the two RBP-binding motifs in the RNA were then determined as a function of the normalized distance from the geometric center of the speckle ($D_{center,\ norm}$, Figure 2C, (i)) for individual speckles (Figure S4, (3 and 4)). The normalized radial distributions were then averaged across the population of speckles (Figure S4, (5)). Strikingly, this analysis demonstrated in a statistically significant way that the SRSF1 motif-rich region is distributed closer to the center of the speckle compared to the hnRNPA1 motif-rich region (Figures 2E and 2F). We also analyzed the two biological replicates individually and observed the same trend in the distribution of SRSF1 and hnRNPA1 motif-rich regions despite the larger standard deviation due to smaller sample size (Data S1). These results indicate that the intra-organelle RNA organization model applies to nuclear speckles.

We remark that the RNA distribution within speckles exhibited some heterogeneity (Figure S5): while in some speckles RNA was mainly localized to the periphery, in others it was mixed into the internal regions (Figure S5B). While we do not know the exact cause of this heterogeneity (see discussion in the following), we analyzed the radial distribution of RNA signals in these two speckle subpopulations separately. As expected, the overall $D_{center,\ norm}$ of both RNA motifs are smaller in the mixed population compared to the periphery-localized population. However, the same orientation of SRSF1 and hnRNPA1 motifs is robustly maintained in both subpopulations (Figure S5C). For simplicity, we report all other analyses on the entire population of speckles, without separating into these two types.

In an alternative analysis, we calculated the radial intensity distributions of the two RNA signals as a function of the normalized distance from the edge of the speckle ($D_{edge,\ norm}$, Figure 2C, (ii), Figure S4, (4 and 5)). In agreement with our first analysis, this analysis demonstrated that the SRSF1 motif-rich region is distributed further away from the edge of the speckle, i.e., closer to the center of the speckle, compared to the hnRNPA1 motif-rich region (Figures 2G and 2H).

Finally, we also estimated the mean absolute radial distance difference between the two regions ($D_{center,abs}$ and $D_{edge,abs}$). We found this distance to be 15–25 nm (Figures 2D, S6D, and S6E), consistent with the typical physical size of an RNA molecule (~40–100 nm).[38–41]

Together, these analyses show that different sequence domains in an RNA molecule can exhibit differential spatial distributions in nuclear speckles, in agreement with the intra-speckle organization model (Figure 1).

Validation of intra-speckle RNA organization

We performed several experiments to validate the intra-speckle RNA organization. First, to rule out any potential imaging artifacts due to the choice of fluorophores and chromatic offsets, we reversed the FISH labeling scheme, by labeling SRSF1 motifs with AF647 and hnRNPA1 motifs with CF568. We observed the same intramolecular organization trend, using both analysis methods (Figure S7A–S7D).

Next, we tested whether the measured mean radial distance difference between the two regions can quantitatively reflect the physical distance between the two labeled regions on the transcript, given our imaging resolution. We quantified the radial distribution and absolute mean radial distance for two additional cases. (1) We mixed AF647-labeled and CF568-labeled probes, both targeting the SRSF1 motifs. As expected, we observed a near zero (4.5 $\pm$ 2.5 nm) difference in the mean radial distance difference between the signals (Figures 2D and S6). (2) We generated an additional construct $MUT_{S1\text{-}spacer\text{-}H1}$ by introducing a neutral 720-nt spacer between the SRSF1 and hnRNPA1 motif-rich regions (Figure 2A). Introduction of the spacer did not change the splicing outcome (Figure S2C). We found that $MUT_{S1\text{-}spacer\text{-}H1}$ demonstrated the same intra-speckle organization as $MUT_{S1\text{-}H1}$ (Figures 2I–2L), with a higher mean radial distance difference of 30–50 nm between the SRSF1 motif-rich and hnRNPA1 motif-rich regions (Figures 2D and S6). The observed trends are also reproduced when the biological replicates were analyzed separately (Data S1). In summary, the absolute mean radial distance difference between the two labeled regions increased as the number of nucleotides between the two labeled regions increased (Figure 2D), confirming that our imaging resolution allows quantification of the physical distance between the two labeled regions on the transcript. In addition, the observed increase argues against the possibility that the FISH signal originates from spliced products, as the presence of a linker should make no difference in the distribution of two physically separated RNA fragments.

$MUT_{S1\text{-}H1}$ contains repeat sequences of SR and hnRNP binding motifs. To rule out the possibility that the intra-speckle RNA organization is an artifact of these repetitions, we synthesized construct $MUT_{S1\text{-}H1,NR}$ (Figure S8A), where we randomly mutated 30% of the nucleotides in the SR and hnRNP motif-rich regions, resulting in "non-repeat" (NR) sequences. This construct is still enriched in SRSF1 motifs in the exon and in hnRNPA1 motifs in the intron (Figures S8B and S8C), but devoid of repeats, as measured by BLAST. RNA transcripts from this construct demonstrated the same splicing behavior as $MUT_{S1\text{-}H1}$ (Figure S2B). Importantly, they also demonstrated similar intra-speckle RNA organization (Figures S8D–S8G). These results confirmed that the intra-speckle RNA organization is driven by the presence of SRSF1- and hnRNPA1-binding motifs, and not by sequence repetition.

Even though our RT-PCR results indicate that the second intron of $MUT_{S1\text{-}H1}$ is mostly unspliced (Figure S2B), a weak band suggests the presence of a minor population of spliced products. To further rule out the possibility that the observed differential distribution is due to separation of the two motifs from this minor population, we used the splicing inhibitor Pladienolide B. After treatment with the inhibitor, the minor splicing products are no longer visible in RT-PCR (Figure S2B). Consistent with earlier reports,[43] speckle size increased in the presence of Pladienolide B; however, the ellipticity and regularity of the speckle surface were not significantly affected (Figure S9), suggesting that our analysis pipeline can be applied without further modifications. We therefore proceeded to image $MUT_{S1\text{-}H1}$ in the presence of Pladienolide B (Figure S10), applying the same speckle size and ellipticity cutoffs for an unbiased comparison of samples. We found that the organization of the SRSF1- and hnRNPA1-binding motifs remains mostly the same after Pladienolide B treatment. This suggests that the observed intramolecular organization is not due to any artifact caused by a minor population of spliced products or intron lariats.

Together, these results further validate that RNAs exhibit distinctive intra-speckle organization, with SRSF1 motif-rich regions positioned closer to the speckle center compared with hnRNPA1 motif-rich regions.

Unspliced pre-mRNA exhibits similar intra-speckle organization

We next examined the intra-speckle organization of transcripts from $WT_{S1\text{-}H1}$ construct using SMLM imaging, which contains a complete set of bona fide splice sites, therefore better mimicking endogenous transcripts (Figure 3A). Since this construct undergoes rapid splicing, we again used Pladieonolide B to ensure that we imaged pre-mRNAs containing both SRSF1 and hnRNPA1 motifs on the same molecule and not spliced products or intron lariats. RT-PCR results indicate an almost complete lack of any splicing activity (Figure S2A). After imaging and applying our analysis pipeline, we found that the SRSF1 motif and hnRNPA1 motif-rich regions of $WT_{S1\text{-}H1}$ pre-mRNA exhibit the same intra-speckle organization as that of $MUT_{S1\text{-}H1}$ RNA (Figures 3B–3E). This suggests that intra-speckle organization can also apply to endogenous speckle-localized transcripts.

Intra-speckle organization is not due to transcription order

Actively transcribed genes are found to be associated with speckle periphery.[17] One possible explanation for the organization we observed is that the hnRNPA1 motif-rich region, being downstream of the SRSF1 motif-rich region, is transcribed later and is therefore closer to the transcription site positioned outside nuclear speckles. However, we expect that, at 2 h after induction, most transcripts are no longer associated with the DNA and that any orientation that is present during transcription cannot persist for that long.

Nevertheless, to rule out transcription order as a cause, we performed two additional experiments. In the first experiment, we designed construct $WT_{H1\text{-}S1}$ in which the hnRNPA1-binding motifs were moved to the intron upstream of the SRSF1 motif-containing middle exon ($WT_{H1\text{-}S1}$, Figure 3A). The $WT_{H1\text{-}S1}$ construct was spliced similarly to the $WT_{S1\text{-}H1}$ construct (Figure S2D), and we imaged the pre-mRNA from this construct in the presence of Pladienolide B. In the second experiment, we imaged $MUT_{S1\text{-}H1}$ RNA in the presence of the transcription

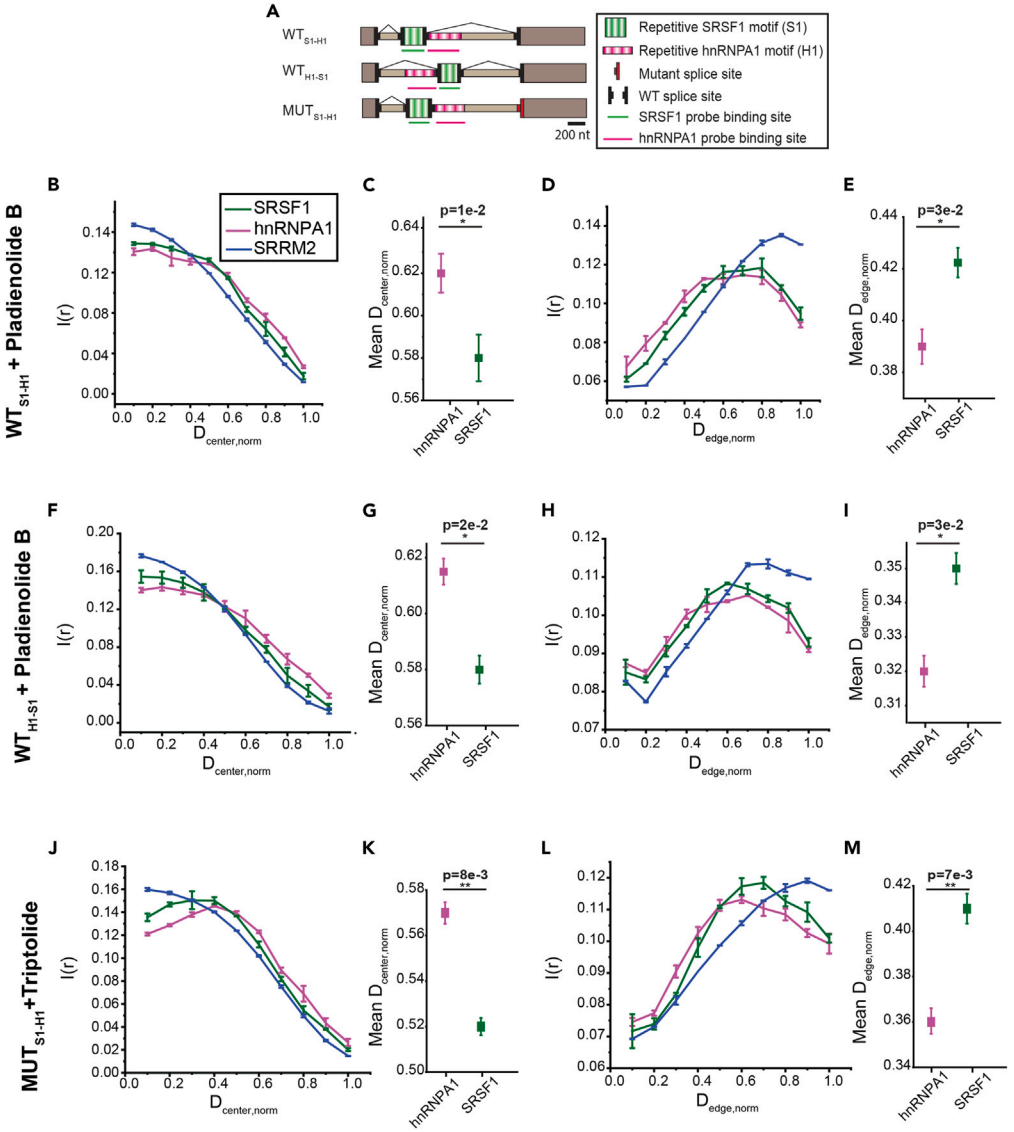

Figure 3. Effect of restored 3′ active splice site and transcription on intra-speckle organization of RNAs containing SRSF1 motifs in exon and hnRNPA1 motifs in intron

(A) Schematic illustration of $WT_{S1\text{-}H1}$, $WT_{H1\text{-}S1}$, and $MUT_{S1\text{-}H1}$.

(B and D) Population distribution of SRSF1 and hnRNPA1 motif signals as a function of the normalized distance from the center of the speckle (B) and edge of the speckle (D) for $WT_{S1\text{-}H1}$ in the presence of Pladienolide B.

(C and E) Population-weighted mean normalized distance of SRSF1 and hnRNPA1 signal from the center of speckle (C) and edge of the speckle (E) for each speckle for $WT_{S1\text{-}H1}$ in the presence of Pladienolide B.

(F and H) Population distribution of SRSF1 and hnRNPA1 motif signals as a function of the normalized distance from the center of the speckle (F) and edge of the speckle (H) for $WT_{H1\text{-}S1}$ in the presence of Pladienolide B.

(G and I) Population-weighted mean normalized distance of SRSF1 and hnRNPA1 signal from the center of speckle (G) and edge of the speckle (I) for each speckle for $WT_{H1\text{-}S1}$ in the presence of Pladienolide B.

(J and L) Population distribution of SRSF1 and hnRNPA1 motif signals as a function of the normalized distance from the center of the speckle (J) and edge of the speckle (L) for $MUT_{S1\text{-}H1}$ in the presence of Triptolide.

(K and M) Population-weighted mean normalized distance of SRSF1 and hnRNPA1 signal from the center of speckle (K) and edge of the speckle (M) for each speckle $MUT_{S1\text{-}H1}$ in the presence of Triptolide. Error bars in the population vs. distance plots report the standard deviation from two replicates, each replicate containing at least 36–48 nuclear speckles collected from 3 to 4 cells. Scatterplots are generated by combining all nuclear speckles (72–96) from two replicates. Values in scatterplot represent mean ± SEM. *p* values in the scatterplots are calculated with paired sample Wilcoxon signed rank test (one-sided), with $*p < 5e\text{-}2$, $**p < 1e\text{-}2$, $***p < 1e\text{-}3$. Replicates are biological replicates collected starting from different dishes of cells and measured on different days.

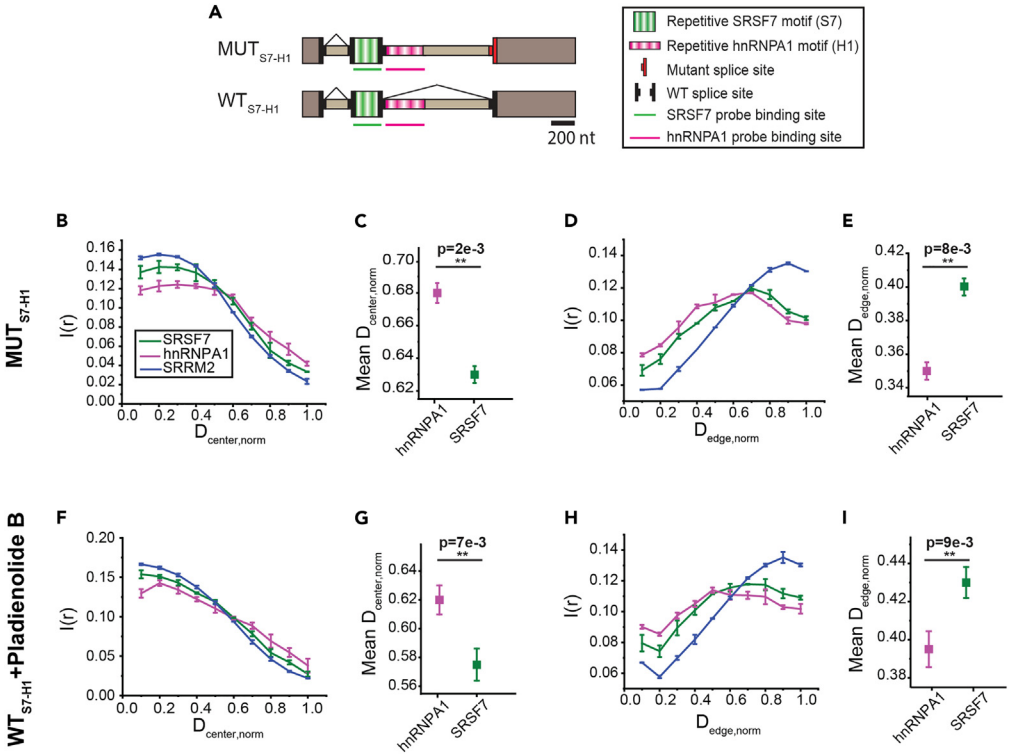

Figure 4. Intra-speckle organization of RNAs containing SRSF7 motifs in exon and hnRNPA1 motifs in intron

(A) Schematic illustration of $MUT_{S7\text{-}H1}$ and $WT_{S7\text{-}H1}$ constructs.

(B and D) Population distribution of SRSF7 and hnRNPA1 motif signals for $MUT_{S7\text{-}H1}$ as a function of the normalized distance from the center of the speckle (B) and edge of the speckle (D).

(C and E) Population-weighted mean normalized distance of SRSF7 and hnRNPA1 signal from the center of speckle (C) and edge of speckle (E) for each speckle for $MUT_{S7\text{-}H1}$.

(F and H) Population distribution of SRSF7 and hnRNPA1 motif signals for $WT_{S7\text{-}H1}$ in the presence of Pladienolide B as a function of the normalized distance from the center of the speckle (F) and edge of the speckle (H).

(G and I) Population-weighted mean normalized distance of SRSF7 and hnRNPA1 signal from the center of speckle (G) and edge of speckle (I) for each speckle for $WT_{S7\text{-}H1}$ in the presence of Pladienolide B. Error bars in the population vs. distance plots report the standard deviation from two replicates, each replicate containing at least 48–60 nuclear speckles collected from 4 to 5 cells. Scatterplots are generated by combining all nuclear speckles (96–120) from two replicates. Values in scatterplot represent mean ± SEM. *p* values in the scatterplots are calculated with paired sample Wilcoxon signed rank test (one-sided), with $*p < 5e\text{-}2$, $**p < 1e\text{-}2$, $***p < 1e\text{-}3$. Replicates are biological replicates collected starting from different dishes of cells and measured on different days.

inhibitor Triptolide. Diffraction-limited fluorescence imaging confirms localization of $MUT_{S1\text{-}H1}$ transcripts to nuclear speckles in the presence of transcription inhibition (Figure S3D). As expected upon transcription inhibition, the speckles became more rounded (Figure S9).[21] We again applied the same speckle size and ellipticity cutoffs for an unbiased comparison of samples.

Importantly, in both cases we observed the same intra-speckle RNA organization, in which the SRSF1 motif-rich region is closer to the speckle center than the hnRNPA1 motif-rich region (Figures 3F–3M). These results provide strong evidence that the intra-speckle organization is independent of the order in which the SRSF1 motif-rich and hnRNPA1 motif-rich regions are transcribed.

RNA transcripts with a combination of SRSF7 and hnRNPA1 motifs exhibit similar intra-speckle organization

To test whether RNA containing other combinations of SR and hnRNP motifs exhibits similar positioning and orientation within nuclear speckles, we replaced the SRSF1 motifs in $MUT_{S1\text{-}H1}$ and $WT_{S1\text{-}H1}$ with SRSF7 motifs to generate $MUT_{S7\text{-}H1}$ and $WT_{S7\text{-}H1}$ (Figure 4A). The splicing behavior of these constructs was similar to that of the SRSF1 motif-containing ones (Figures S2A and S2B). The radial intensity distributions with respect to the center and edge showed that the SRSF7 motif-rich region is closer to the center of nuclear speckles than the hnRNPA1 motif-rich region (Figures 4B–4I), the same trend observed for $MUT_{S1\text{-}H1}$ and $WT_{S1\text{-}H1}$. These results demonstrate that the intra-speckle organization of SR and hnRNP motifs is not specific to the SRSF1-hnRNPA1 combination.

RNA-RBP interaction strength determines RNA organization in nuclear speckle

We hypothesize that the mechanism underlying intra-speckle RNA organization is the multivalent interactions between RNAs with RBPs residing inside and outside nuclear speckles. We therefore expect that weakening RNA-SR protein interaction will lead to the migration of

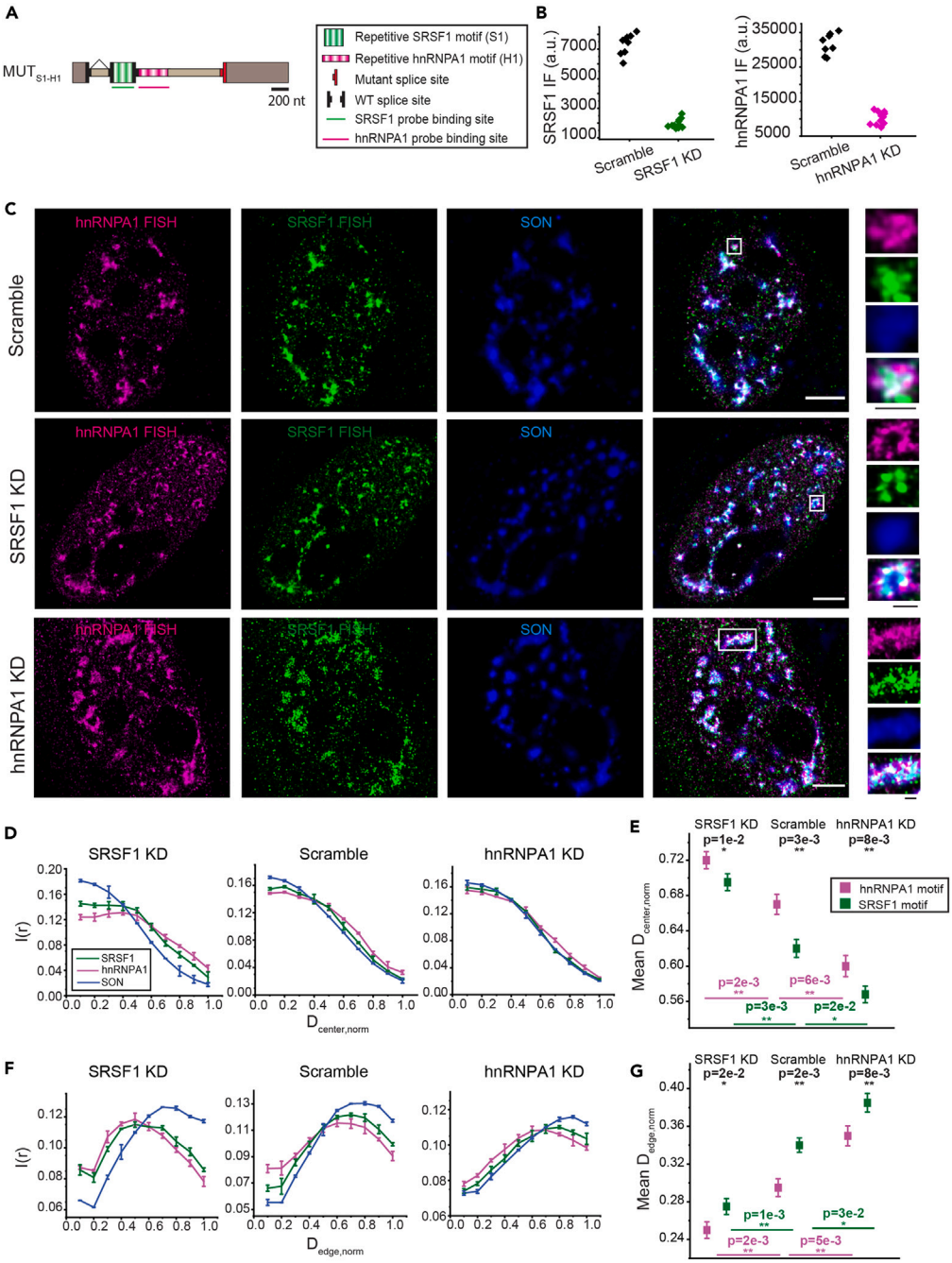

Figure 5. Effect of SRSF1 and hnRNPA1 knockdown on the intra-speckle organization of RNAs containing SRSF1 motifs in exon and hnRNPA1 motifs in intron

(A) Schematic illustration of $MUT_{S1\text{-}H1}$.

(B) Immunofluorescence (IF) quantification of each cell chosen for imaging treated with scramble siRNA, siRNA against SRSF1 and siRNA against hnRNPA1. Immunofluorescence is quantified by staining SRSF1 and hnRNPA1 proteins with their respective antibodies and imaging with a 750 nm laser under scramble and knockdown conditions and computing the average intensity of the whole cell.

(C) Representative SMLM images of $MUT_{S1\text{-}H1}$ treated with scramble siRNA, siRNA against SRSF1 and siRNA against hnRNPA1. FISH signals corresponding to hnRNPA1 and SRSF1 motifs in the RNAs are shown in magenta and green respectively. Immunostaining of scaffold protein SON is shown in blue. Scale bars represent 5 μm (white) and 1 μm (black).

(D and F) Population distribution of SRSF1 and hnRNPA1 motif signals as a function of the normalized distance from the center (D), and from the edge (F) of the speckle for $MUT_{S1\text{-}H1}$ under knockdown conditions.

Figure 5. *Continued*

(E and G) Population-weighted mean normalized distance of SRSF1 and hnRNPA1 signal from the center (E), and from the edge (G) for each speckle for $MUT_{S1\text{-}H1}$ under knockdown conditions. Error bars in the population vs. distance plots report the standard deviation from two replicates, each replicate containing at least 48–72 nuclear speckles collected from 4 to 6 cells. Scatterplots are generated by combining all nuclear speckles (96–144) from two replicates. Values in scatterplot represent mean ± SEM. *p* values in the scatterplots are calculated with paired sample Wilcoxon signed rank test (black, one-sided) and two sample t test (magenta and green, one-sided), with $*p < 5e\text{-}2$, $**p < 1e\text{-}2$, $***p < 1e\text{-}3$. Replicates are biological replicates collected from different dishes of cells and measured on different days. Also see Figures S11 and S12.

RNAs toward the speckle periphery, whereas weakening RNA-hnRNP protein interaction will lead to the migration of RNAs toward the speckle interior. In addition, weakened RNA-RBP interactions should lead to reduced constraints on RNA orientation, which would be reflected by a reduced difference in intra-speckle positioning of the two motif-rich regions. To test this hypothesis, we perturbed the RNA-RBP interaction in two ways: knocking down RBPs individually (Figure 5) or removing RBP-binding motifs from the RNA individually (Figure 6).

We first measured intra-speckle organization upon small interfering RNA (siRNA)-mediated knockdown of SRSF1 or hnRNPA1 proteins. We achieved 83% ± 5% and 57% ± 8% knockdown efficiency of *SRSF1* and *hnRNPA1* mRNAs, respectively (Figure S11), without observing any significant change in nuclear speckle morphology (Figure S9). We performed SMLM imaging under these knockdown conditions, using $MUT_{S1\text{-}H1}$ as a representative. To choose cells with efficient protein knockdown, hnRNPA1 and SRSF1 proteins were stained with their respective antibodies and imaged with a 750 nm laser. Cells showing significant reduction in immunofluorescence signal compared to cells treated with scramble siRNA were selected (Figure 5B). Confirming our hypothesis, SRSF1 knockdown caused significant migration of RNA transcripts toward the speckle periphery (Figures 5C–5G). Conversely, hnRNPA1 knockdown caused RNA migration toward the speckle interior (Figures 5C–5G). Co-migration of both motifs upon SRSF1 or hnRNPA1 knockdown further supports that the FISH signals are from unspliced RNAs, rather than from spliced products; otherwise, we would expect only SRSF1 motif localization to change upon SRSF1 knockdown and only hnRNPA1 motif localization to change upon hnRNPA1 knockdown. In addition, as predicted, the difference in intra-speckle positioning of the two motif-rich regions was reduced under each knockdown condition. Finally, the trends were reproducible when we reversed the FISH labeling scheme (Figures S7E–S7L).

We extended our siRNA-mediated knockdown experiments to $MUT_{S7\text{-}H1}$. In contrast to $MUT_{S1\text{-}H1}$, SRSF1 knockdown only caused minor outward movement of RNA transcripts from the $MUT_{S7\text{-}H1}$ construct, and no noticeable change in the intra-speckle positioning difference of the two motif-rich regions (Figure S12). This is consistent with the fact that $MUT_{S7\text{-}H1}$'s middle exon does not contain any SRSF1 motifs and should thus be less sensitive to SRSF1 protein knockdown. This minor outward migration might be explained by a slight downregulation (10% ± 9%) of SRSF7 when knocking down SRSF1 (Figure S11). On the other hand, as expected, hnRNPA1 knockdown still led to very similar results to those observed with $MUT_{S1\text{-}H1}$ (migration toward speckle center and smaller difference in positioning between the two motif-rich regions) (Figure S12).

We further modulated the RNA-RBP interactions by removing one of the RBP-binding motifs in the RNA. We generated two size-matching single-motif variants of construct $MUT_{S1\text{-}H1}$: $MUT_{N\text{-}H1}$ containing only an hnRNPA1 motif-rich region and $MUT_{S1\text{-}N}$ containing only an SRSF1 motif-rich region (Figure 6A). $MUT_{N\text{-}H1}$ RNA transcripts lacking the SRSF1-binding motifs showed a migration toward the speckle periphery (Figures 6B–6D, 6G, and 6H), similar to the effect of SRSF1 protein knockdown. In addition, $MUT_{S1\text{-}N}$ RNA transcripts lacking the hnRNPA1-binding motifs showed an inward migration toward the center of the speckle (Figures 6B, 6E–6H), similar to the effect of hnRNPA1 protein knockdown.

Collectively, these results suggest that RNA-RBP interaction strength drives intra-speckle RNA organization. It is interesting to note that knocking down SRSF1 protein or removing SRSF1 motifs from the RNA sequence causes RNA migration to the speckle periphery but not a complete relocation out of speckles. While localization to nuclear speckles depends on multivalent RNA-RBP interactions (such as the SRSF1 motifs), other *cis*-factors on RNA transcripts, such as splice site sequences, also play a role in RNA localization to speckles,[29,44] which can explain the remaining speckle association of $MUT_{N\text{-}H1}$ or upon SRSF1 knockdown. However, addressing the exact sequence determinants of speckle localization is beyond the scope of this manuscript.

A toy model reproduces the intra-speckle RNA organization

Finally, we computationally tested whether RNA-RBP interactions are sufficient for explaining the observed intra-speckle RNA organization. In this simple toy model, we considered four lattice sites, with two sites inside the speckle and two sites outside. We then considered the position and orientation of a 2-block RNA molecule, corresponding to an SR motif-rich region and an hnRNP motif-rich region, leading to a total of 6 configurations (Figure 7A). In each configuration, each block on the RNA molecule can be either bound or unbound by the corresponding protein, leading to 4 binding states per configuration, and 24 energy states in total (Table S1). The relative population of each energy state can be estimated by the dissociation constant (K_d) of each RNA-RBP pair, and the concentration of these RBPs in each location. The intra-speckle positioning of the two regions on the RNA was then estimated using a Boltzmann distribution. The modeling details are described in STAR Methods.

Our simulation recapitulated the differential intra-speckle spatial distribution of the SRSF1 and hnRNPA1 motif-rich regions (Figure 7B). In addition, the model recapitulated the changes of intra-speckle RNA organization upon SRSF1 and hnRNPA1 knockdowns (Figures 7C and 7D) in two aspects: (1) a change in RNA positioning as an entity and (2) a less constrained RNA orientation reflected by a smaller difference in the intra-speckle positioning of the two RBP motifs. Finally, the simulation indicated that the intra-organelle organization applies to a broad range of binding affinities (with K_d ranging from 100 nM to 10 μM) (Figures 7 and S13). In fact, increasing the K_d parameter in our toy model leads to results closer to the experimentally measured values, suggesting that RNA-RBP interactions *in vivo* may be considerably weaker than the *in vitro* measured values,[45,46] possibly due to competition from other cellular proteins.

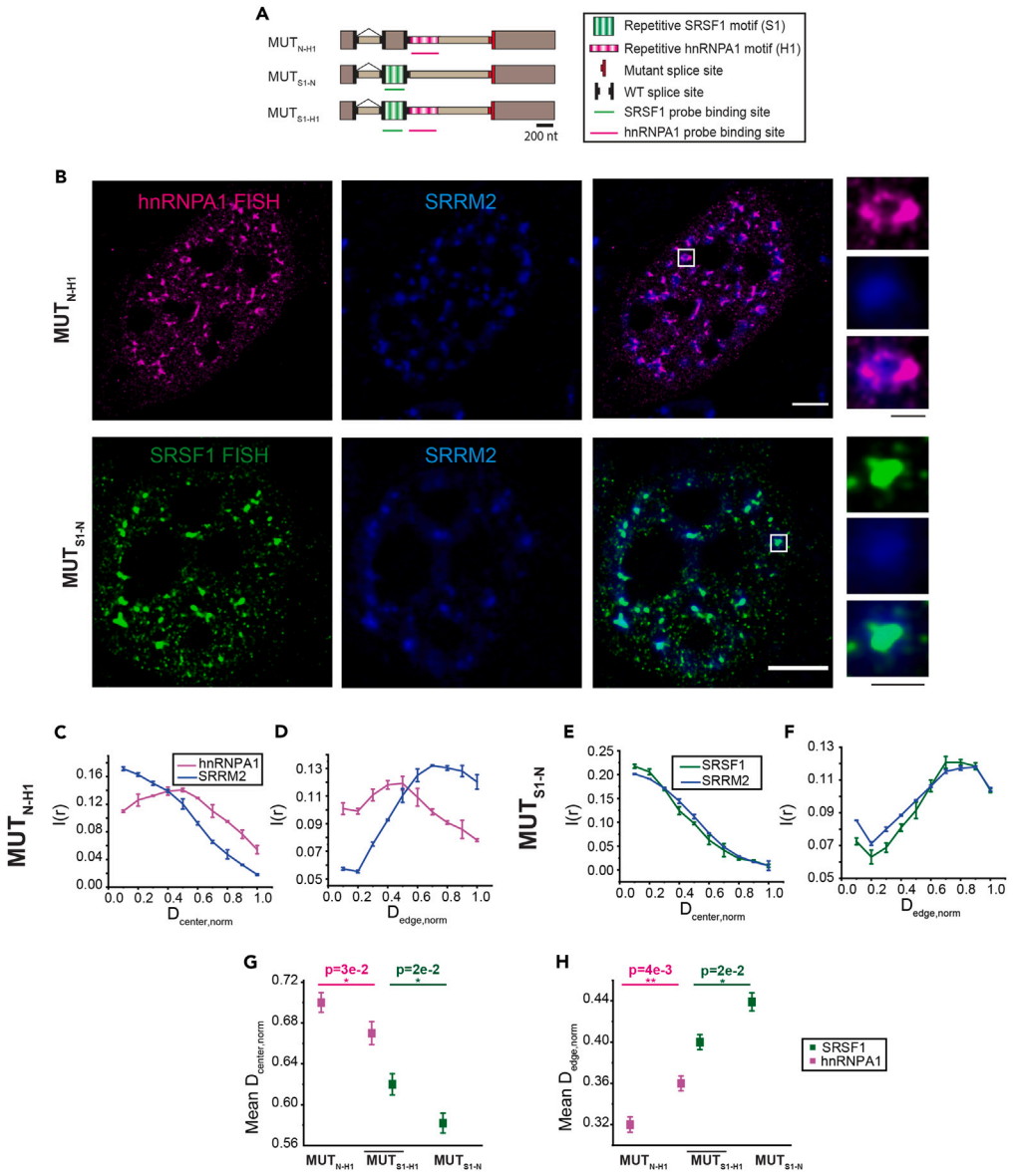

Figure 6. Intra-speckle organization of RNAs from single-motif constructs containing either SRSF1 motifs in exon or hnRNPA1 motifs in intron

(A) Schematic illustration of $MUT_{N\text{-}H1}$, $MUT_{S1\text{-}N}$, and $MUT_{S1\text{-}H1}$ constructs. $MUT_{N\text{-}H1}$ and $MUT_{S1\text{-}N}$ are size-matched variants of construct $MUT_{S1\text{-}H1}$. $MUT_{N\text{-}H1}$ contains hnRNPA1-binding motifs in the intron and a neutral exon. $MUT_{S1\text{-}N}$ contains SRSF1-binding motifs in the exon and a neutral intron.

(B) Representative SMLM image of $MUT_{N\text{-}H1}$ and $MUT_{S1\text{-}N}$. Scale bars represent 5 μm (white) and 1 μm (black).

(C and D) Population distribution of hnRNPA1 motif signals for $MUT_{N\text{-}H1}$ as a function of the normalized distance from the center of the speckle (C) and edge of the speckle (D).

(E and F) Population distribution of SRSF1 motif signals for $MUT_{S1\text{-}N}$ as a function of the normalized distance from the center of the speckle (E) and edge of the speckle (F).

(G and H) Comparison of the population-weighted mean normalized distance of hnRNPA1 and SRSF1 signals from $MUT_{S1\text{-}H1}$ with hnRNPA1 signal from $MUT_{N\text{-}H1}$ and SRSF1 signal from $MUT_{S1\text{-}N}$, respectively from the center of speckle (G) and edge of speckle (H) for each speckle. Error bars in the population vs. distance plots report the standard deviation from two replicates, each replicate containing at least 75–90 nuclear speckles from 5 to 6 cells. Scatterplots are generated by combining all nuclear speckles (150–180) from two replicates. Values in scatterplot represent mean ± SEM. *p* values in the scatterplots are calculated with two sample t test, with $*p < 5e\text{-}2$, $**p < 1e\text{-}2$, $***p < 1e\text{-}3$. Replicates are biological replicates collected from different dishes of cells and measured on different days.

DISCUSSION

In this study, we proposed an intra-organelle RNA organization model and demonstrated it using nuclear speckles as a model system (Figure 1). Specifically, we observed that an SR motif-rich region is localized closer to the speckle center than an hnRNP motif-rich region present

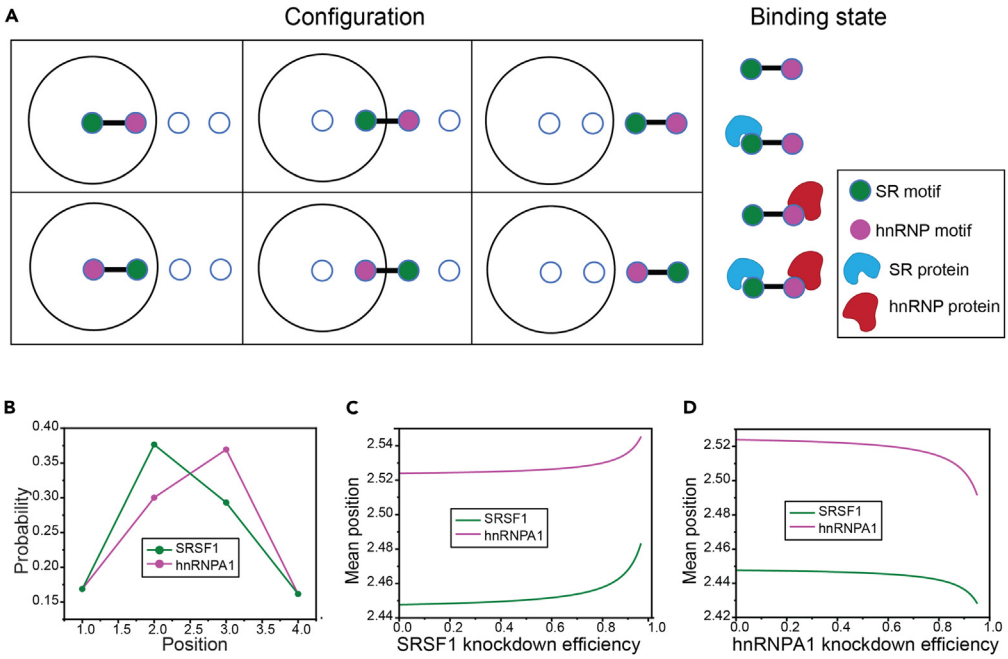

Figure 7. A toy model recapitulated the intra-speckle positioning of SRSF1 and hnRNPA1 motif-rich region of the RNA

(A) Graphical representation of the 6 configurations (3 positions and 2 orientations) of the RNA molecule and 4 binding states. Specifically, the positions of the SRSF1 and hnRNPA1 motif-rich regions can be both inside, both outside, or straddle the speckle interface (one inside and one outside). Each position can have two orientations (SRSF1 motif-rich region inside or hnRNPA1 motif-rich region inside). In each configuration, there are four binding states corresponding to each block on the RNA molecule being either bound or unbound by the corresponding protein.

(B) Probability distribution of position of the SRSF1 and hnRNPA1 motif-rich regions, as predicted by the toy model.

(C and D) Mean positions of SRSF1 and hnRNPA1 motif determined by this model are plotted as a function of SRSF1 (C) and hnRNPA1 (D) knockdown efficiencies. The case here represents K_d = 1 μM. Also see Figure S13 and Table S1.

in the same RNA molecule. Even though our results represent the population average of many RNAs, they are indicative of preferred orientation in individual molecules. To experimentally demonstrate this spatial organization, we engineered reporter constructs that are enriched in SRSF1/7- and hnRNPA1-binding motifs. Such a design guarantees that the intra-speckle organization is primarily driven by interactions with these specific proteins and allowed us to measure the effect of knockdowns. We expect the organization of endogenous RNA transcripts to be determined by the combined interaction with the multitude of RBPs inside and outside speckles.

We observed heterogeneity in the intra-speckle RNA distribution: while in some speckles RNAs are exclusively localized to the periphery, in others they are more mixed into speckles and broadly distributed in the speckle outer shell. While we do not know the exact cause of this heterogeneity, we speculate several possible contributing factors. First, heterogeneity in the abundance of SRSF1 proteins in nuclear speckles could be a reason; this is supported by the observation that upon SRSF1 knockdown, RNAs are exclusively peripheral in almost all speckles. Speckle fusing could be another reason; indeed, we noticed that very large and irregular speckles, which probably arise through fusing, tend to be associated with RNAs mixed into speckles (Figure S5B). A final reason could be the distance from the gene foci, as earlier studies suggest that RNAs localizing to speckles co-transcriptionally are likely more on the speckle periphery and closer to the gene foci, whereas post-transcriptionally localizing RNA can be more in the speckle interior.[47] The last reason, however, is unlikely to apply here: the speckle-localized transcripts in the current study should be mostly post-transcriptional (due to the stalling mutation in the MUT constructs and due to the use of splicing inhibition in the WT constructs). Moreover, a similar heterogeneity was observed previously for the intra-speckle distribution of the *MALAT1* RNA and snRNP components,[16] which are not linked to any particular gene foci.

Intra-organelle RNA organization is likely not restricted to nuclear speckles and can potentially apply to any membraneless organelle enriched in certain RBPs but depleted for others. Indeed, our toy model shows that RNA organization can arise from an RBP concentration difference between the inside and outside of membraneless organelles. In addition, it was reported that a long mRNA, *AHNAK* (>18 kb), which localizes to cytoplasmic stress granules, is more often observed with its 3′ end extending out of stress granules and its 5′ end residing in stress granules, compared to the other orientation.[15] While no mechanism for this observation was provided, this observation suggests that non-random RNA organization within other membraneless organelles is possible and remains to be further investigated.

While nuclear speckles are not known to rely on any specific RNA to assemble, their structural stability depends on the presence of nuclear RNA in general. Indeed, a recent study showed that depletion of nuclear RNA leads to loss of nuclear speckles and causes SON and SRRM2 to reorganize into a few large protein aggregates.[11] Our observation that RNAs exhibit preferential intra-speckle organization might explain the importance of RNA molecules in maintaining the structural integrity of nuclear speckles. Specifically, through their interactions with proteins

inside and outside of nuclear speckles, RNA molecules might be oriented similarly to amphiphilic polymers at the water-oil interface and help prevent the formation of SON or SRRM2 protein aggregates. A related idea was recently proposed in the context of proteins, where the MEG-3 protein was suggested to serve as a Pickering agent to maintain an appropriate size distribution of P granules in *C. elegans*, by localizing to their surface and reducing surface tension.[48]

Finally, our results suggest that nuclear speckles might play a role in facilitating splicing through organizing pre-mRNA substrates. SR and hnRNP proteins are important splicing regulators[49,50] showing antagonistic effects on splicing.[51] While SR binding motifs are more enriched in exons, hnRNP binding motifs are more enriched in introns.[33] We hypothesize that this specific sequence arrangement can enhance splicing by driving intra-speckle organization of pre-mRNA substrates.[52] Specifically, a splice site found between an SR motif-rich exon and an hnRNP motif-rich intron will be positioned at the speckle outer layer, possibly providing better spatial overlap with spliceosomal components, which are known to also localize at the outer layer,[16] thereby favoring the splicing reaction. However, future experiments are needed to demonstrate a causal relationship between intra-speckle RNA organization and splicing activity.

Limitations of the study

In this study, we chose to perform 2D-SMLM imaging on the middle plane of speckles within a single cell. This two-dimensional information was sufficient to quantitatively demonstrate the organization of RNA molecules within speckles. While in principle three-dimensional imaging could be more informative, technical limitations of current methods pose some challenges. First, 3D-SMLM microscopes using cylindrical lenses typically provide a reliable z range of 400–800 nm, which is insufficient to capture the entire z range of a typical speckle (a few hundred nanometers to a few microns). Moreover, the z resolution is typically 2–3 fold worse than the xy resolution, which may comprise our ability to resolve small distance between the two RBP motifs. Finally, in our previous work using structural illumination microscopy (which also has lower z resolution than xy resolution), differential organization of various speckle components was better resolved using 2D images of the middle plane of speckles than with 3D images.[16]

While our results are indicative of preferred orientation in individual molecules, current imaging resolution does not allow a full description of the detailed conformation or morphology of individual RNA molecules. It would be interesting to explore the organization behavior using other complementary techniques, such as single-molecule FISH, live-cell imaging, or cryo-electron tomography. Each technique comes with its advantages and limitations, and combining several techniques could provide a more complete picture of speckle organization, and possibly its functional implications on RNA processing.

Our study focuses on transiently transfected synthetic reporter constructs. It would be interesting to explore whether endogenous speckle-localized transcripts exhibit the same intra-speckle RNA organization. Our results with $WT_{S1\text{-}H1}$ suggest that this is the case. Endogenous transcripts present additional challenges: some are not very highly expressed, some are not localized to speckles,[19,24] and many contain additional sequence elements (cryptic splice sites, additional RNA binding motifs) that can complicate the interpretation of the imaging results. In addition, splicing is usually fast, leading to a heterogeneous population of RNA products.

STAR★METHODS

Detailed methods are provided in the online version of this paper and include the following:

- KEY RESOURCES TABLE
- RESOURCE AVAILABILITY
  - Lead contact
  - Materials availability
  - Data and code availability
- EXPERIMENTAL MODEL AND STUDY PARTICIPANT DETAILS
  - Cell lines
- METHOD DETAILS
  - Plasmid design and construction
  - Cell culture, transfection, and drug treatments
  - RT-PCR for biochemical assays
  - siRNA-mediated knockdown
  - qPCR quantification for knockdown efficiency
  - Labeling of FISH probes and secondary antibodies
  - RNA FISH and immunostaining
  - Imaging and image reconstruction
  - Data analysis
  - Modeling details
- QUANTIFICATION AND STATISTICAL ANALYSIS

SUPPLEMENTAL INFORMATION

Supplemental information can be found online at https://doi.org/10.1016/j.isci.2024.109603.

ACKNOWLEDGMENTS

This project was supported by the NIH Director's New Innovator Award (1DP2GM128185-01) to J.F., a Simons Investigator Award and NSF MCB-2226731 to O.R., NSF MCB-2246530 to J.F. and O.R., a Yen Foundation Fellowship to S.P., and a Life Sciences Research Foundation Fellowship from Additional Ventures to S.E.L.

AUTHOR CONTRIBUTIONS

Conceptualization: J.F., O.R., S.P., M.A.A., S.E.L., L.W. Experiment and analysis: S.P., M.A.A., L.W., S.E.L., J.Z., X.W. Supervision: J.F., O.R. Writing: J.F., O.R., S.P., L.W., M.A.A., S.E.L.

DECLARATION OF INTERESTS

The authors declare no competing interests.

Received: August 9, 2023
Revised: January 5, 2024
Accepted: March 25, 2024
Published: March 27, 2024

REFERENCES

1. Dundr, M. (2012). Nuclear bodies: multifunctional companions of the genome. Curr. Opin. Cell Biol. *24*, 415–422. https://doi.org/10.1016/j.ceb.2012.03.010.
2. Zhu, L., and Brangwynne, C.P. (2015). Nuclear bodies: the emerging biophysics of nucleoplasmic phases. Curr. Opin. Cell Biol. *34*, 23–30. https://doi.org/10.1016/j.ceb.2015.04.003.
3. Buchan, J.R., and Parker, R. (2009). Eukaryotic stress granules: the ins and outs of translation. Mol. Cell *36*, 932–941. https://doi.org/10.1016/j.molcel.2009.11.020.
4. Decker, C.J., and Parker, R. (2012). P-bodies and stress granules: possible roles in the control of translation and mRNA degradation. Cold Spring Harbor Perspect. Biol. *4*, a012286. https://doi.org/10.1101/cshperspect.a012286.
5. Banani, S.F., Lee, H.O., Hyman, A.A., and Rosen, M.K. (2017). Biomolecular condensates: organizers of cellular biochemistry. Nat. Rev. Mol. Cell Biol. *18*, 285–298. https://doi.org/10.1038/nrm.2017.7.
6. Banani, S.F., Rice, A.M., Peeples, W.B., Lin, Y., Jain, S., Parker, R., and Rosen, M.K. (2016). Compositional Control of Phase-Separated Cellular Bodies. Cell *166*, 651–663. https://doi.org/10.1016/j.cell.2016.06.010.
7. Hyman, A.A., Weber, C.A., and Jülicher, F. (2014). Liquid-liquid phase separation in biology. Annu. Rev. Cell Dev. Biol. *30*, 39–58. https://doi.org/10.1146/annurev-cellbio-100913-013325.
8. Guo, Q., Shi, X., and Wang, X. (2021). RNA and liquid-liquid phase separation. Noncoding. RNA Res. *6*, 92–99. https://doi.org/10.1016/j.ncrna.2021.04.003.
9. Molliex, A., Temirov, J., Lee, J., Coughlin, M., Kanagaraj, A.P., Kim, H.J., Mittag, T., and Taylor, J.P. (2015). Phase separation by low complexity domains promotes stress granule assembly and drives pathological fibrillization. Cell *163*, 123–133. https://doi.org/10.1016/j.cell.2015.09.015.
10. Lin, Y., Protter, D.S.W., Rosen, M.K., and Parker, R. (2015). Formation and Maturation of Phase-Separated Liquid Droplets by RNA-Binding Proteins. Mol. Cell *60*, 208–219. https://doi.org/10.1016/j.molcel.2015.08.018.
11. Decker, C.J., Burke, J.M., Mulvaney, P.K., and Parker, R. (2022). RNA is required for the integrity of multiple nuclear and cytoplasmic membrane-less RNP granules. EMBO J. *41*, e110137. https://doi.org/10.15252/embj.2021110137.
12. Fare, C.M., Villani, A., Drake, L.E., and Shorter, J. (2021). Higher-order organization of biomolecular condensates. Open Biol. *11*, 210137. https://doi.org/10.1098/rsob.210137.
13. West, J.A., Mito, M., Kurosaka, S., Takumi, T., Tanegashima, C., Chujo, T., Yanaka, K., Kingston, R.E., Hirose, T., Bond, C., et al. (2016). Structural, super-resolution microscopy analysis of paraspeckle nuclear body organization. J. Cell Biol. *214*, 817–830. https://doi.org/10.1083/jcb.201601071.
14. Trcek, T., Douglas, T.E., Grosch, M., Yin, Y., Eagle, W.V.I., Gavis, E.R., Shroff, H., Rothenberg, E., and Lehmann, R. (2020). Sequence-Independent Self-Assembly of Germ Granule mRNAs into Homotypic Clusters. Mol. Cell *78*, 941–950.e12. https://doi.org/10.1016/j.molcel.2020.05.008.
15. Moon, S.L., Morisaki, T., Khong, A., Lyon, K., Parker, R., and Stasevich, T.J. (2019). Multicolour single-molecule tracking of mRNA interactions with RNP granules. Nat. Cell Biol. *21*, 162–168. https://doi.org/10.1038/s41556-018-0263-4.
16. Fei, J., Jadaliha, M., Harmon, T.S., Li, I.T.S., Hua, B., Hao, Q., Holehouse, A.S., Reyer, M., Sun, Q., Freier, S.M., et al. (2017). Quantitative analysis of multilayer organization of proteins and RNA in nuclear speckles at super resolution. J. Cell Sci. *130*, 4180–4192. https://doi.org/10.1242/jcs.206854.
17. Faber, G.P., Nadav-Eliyahu, S., and Shav-Tal, Y. (2022). Nuclear speckles - a driving force in gene expression. J. Cell Sci. *135*, jcs259594. https://doi.org/10.1242/jcs.259594.
18. Ha, M. (2020). Transcription boosting by nuclear speckles. Nat. Rev. Mol. Cell Biol. *21*, 64–65. https://doi.org/10.1038/s41580-019-0203-6.
19. Kim, J., Venkata, N.C., Hernandez Gonzalez, G.A., Khanna, N., and Belmont, A.S. (2020). Gene expression amplification by nuclear speckle association. J. Cell Biol. *219*, e201904046. https://doi.org/10.1083/jcb.201904046.
20. Bhat, P., Chow, A., Emert, B., Ettlin, O., Quinodoz, S.A., Takei, Y., Huang, W., Blanco, M.R., and Guttman, M. (2023). 3D genome organization around nuclear speckles drives mRNA splicing efficiency. Preprint at bioRxiv. https://doi.org/10.1101/2023.01.04.522632.
21. Spector, D.L., and Lamond, A.I. (2011). Nuclear Speckles. Cold Spring Harbor Perspect. Biol. *3*, a000646. https://doi.org/10.1101/cshperspect.a000646.
22. Hutchinson, J.N., Ensminger, A.W., Clemson, C.M., Lynch, C.R., Lawrence, J.B., and Chess, A. (2007). A screen for nuclear transcripts identifies two linked noncoding RNAs associated with SC35 splicing domains. BMC Genom. *8*, 39. https://doi.org/10.1186/1471-2164-8-39.
23. Shepard, P.J., and Hertel, K.J. (2009). The SR protein family. Genome Biol. *10*, 242. https://doi.org/10.1186/gb-2009-10-10-242.
24. Barutcu, A.R., Wu, M., Braunschweig, U., Dyakov, B.J.A., Luo, Z., Turner, K.M., Durbic, T., Lin, Z.-Y., Weatheritt, R.J., Maass, P.G., et al. (2022). Systematic mapping of nuclear domain-associated transcripts reveals speckles and lamina as hubs of functionally distinct retained introns. Mol. Cell *82*, 1035–1052.e9. https://doi.org/10.1016/j.molcel.2021.12.010.
25. Tripathi, V., Song, D.Y., Zong, X., Shevtsov, S.P., Hearn, S., Fu, X.-D., Dundr, M., and Prasanth, K.V. (2012). SRSF1 regulates the assembly of pre-mRNA processing factors in nuclear speckles. Mol. Biol. Cell *23*, 3694–3706. https://doi.org/10.1091/mbc.E12-03-0206.
26. Mintz, P.J., Patterson, S.D., Neuwald, A.F., Spahr, C.S., and Spector, D.L. (1999). Purification and biochemical characterization of interchromatin granule clusters. EMBO J. *18*, 4308–4320. https://doi.org/10.1093/emboj/18.15.4308.
27. Saitoh, N., Spahr, C.S., Patterson, S.D., Bubulya, P., Neuwald, A.F., and Spector, D.L. (2004). Proteomic analysis of interchromatin granule clusters. Mol. Biol. Cell *15*, 3876–

3890. https://doi.org/10.1091/mbc.e04-03-0253.
28. Dopie, J., Sweredoski, M.J., Moradian, A., and Belmont, A.S. (2020). Tyramide signal amplification mass spectrometry (TSA-MS) ratio identifies nuclear speckle proteins. J. Cell Biol. *219*, e201910207. https://doi.org/10.1083/jcb.201910207.
29. Dias, A.P., Dufu, K., Lei, H., and Reed, R. (2010). A role for TREX components in the release of spliced mRNA from nuclear speckle domains. Nat. Commun. *1*, 97. https://doi.org/10.1038/ncomms1103.
30. Neugebauer, K.M., and Roth, M.B. (1997). Distribution of pre-mRNA splicing factors at sites of RNA polymerase II transcription. Genes Dev. *11*, 1148–1159. https://doi.org/10.1101/gad.11.9.1148.
31. Abdrabou, A., and Wang, Z. (2021). Regulation of the nuclear speckle localization and function of Rac1. Faseb. J. *35*, e21235. https://doi.org/10.1096/fj.202001694R.
32. Arias, M.A., Lubkin, A., and Chasin, L.A. (2015). Splicing of designer exons informs a biophysical model for exon definition. RNA *21*, 213–229. https://doi.org/10.1261/rna.048009.114.
33. Fairbrother, W.G., Yeh, R.-F., Sharp, P.A., and Burge, C.B. (2002). Predictive identification of exonic splicing enhancers in human genes. Science *297*, 1007–1013. https://doi.org/10.1126/science.1073774.
34. Fu, X.-D., and Ares, M. (2014). Context-dependent control of alternative splicing by RNA-binding proteins. Nat. Rev. Genet. *15*, 689–701. https://doi.org/10.1038/nrg3778.
35. Ilik, İ.A., Malszycki, M., Lübke, A.K., Schade, C., Meierhofer, D., and Aktaş, T. (2020). SON and SRRM2 are essential for nuclear speckle formation. Elife *9*, e60579. https://doi.org/10.7554/eLife.60579.
36. Das, R., Dufu, K., Romney, B., Feldt, M., Elenko, M., and Reed, R. (2006). Functional coupling of RNAP II transcription to spliceosome assembly. Genes Dev. *20*, 1100–1109. https://doi.org/10.1101/gad.1397406.
37. Gozani, O., Patton, J.G., and Reed, R. (1994). A novel set of spliceosome-associated proteins and the essential splicing factor PSF bind stably to pre-mRNA prior to catalytic step II of the splicing reaction. EMBO J. *13*, 3356–3367.
38. Gopal, A., Zhou, Z.H., Knobler, C.M., and Gelbart, W.M. (2012). Visualizing large RNA molecules in solution. RNA *18*, 284–299. https://doi.org/10.1261/rna.027557.111.
39. Lubeck, E., and Cai, L. (2012). Single-cell systems biology by super-resolution imaging and combinatorial labeling. Nat. Methods *9*, 743–748. https://doi.org/10.1038/nmeth.2069.
40. Björk, P., and Wieslander, L. (2015). The Balbiani Ring Story: Synthesis, Assembly, Processing, and Transport of Specific Messenger RNA-Protein Complexes. Annu. Rev. Biochem. *84*, 65–92. https://doi.org/10.1146/annurev-biochem-060614-034150.
41. Adivarahan, S., Kalhara Abeykoon, A., and Zenklusen, D. (2021). Single-molecule imaging suggests compact and spliceosome dependent organization of long introns. Preprint at bioRxiv. https://doi.org/10.1101/2021.10.27.466141.
42. Rust, M.J., Bates, M., and Zhuang, X. (2006). Sub-diffraction-limit imaging by stochastic optical reconstruction microscopy (STORM). Nat. Methods *3*, 793–795. https://doi.org/10.1038/nmeth929.
43. Carvalho, T., Martins, S., Rino, J., Marinho, S., and Carmo-Fonseca, M. (2017). Pharmacological inhibition of the spliceosome subunit SF3b triggers exon junction complex-independent nonsense-mediated decay. J. Cell Sci. *130*, 1519–1531. https://doi.org/10.1242/jcs.202200.
44. Melcák, I., Melcáková, S., Kopský, V., Vecerová, J., and Raska, I. (2001). Prespliceosomal assembly on microinjected precursor mRNA takes place in nuclear speckles. Mol. Biol. Cell *12*, 393–406. https://doi.org/10.1091/mbc.12.2.393.
45. Cho, S., Hoang, A., Sinha, R., Zhong, X.-Y., Fu, X.-D., Krainer, A.R., and Ghosh, G. (2011). Interaction between the RNA binding domains of Ser-Arg splicing factor 1 and U1-70K snRNP protein determines early spliceosome assembly. Proc. Natl. Acad. Sci. USA *108*, 8233–8238. https://doi.org/10.1073/pnas.1017700108.
46. Burd, C.G., and Dreyfuss, G. (1994). RNA binding specificity of hnRNP A1: significance of hnRNP A1 high-affinity binding sites in pre-mRNA splicing. EMBO J. *13*, 1197–1204. https://doi.org/10.1002/j.1460-2075.1994.tb06369.x.
47. Hall, L.L., Smith, K.P., Byron, M., and Lawrence, J.B. (2006). The Molecular Anatomy of a Speckle. Anat. Rec. A Discov. Mol. Cell. Evol. Biol. *288*, 664–675. https://doi.org/10.1002/ar.a.20336.
48. Folkmann, A.W., Putnam, A., Lee, C.F., and Seydoux, G. (2021). Regulation of biomolecular condensates by interfacial protein clusters. Science *373*, 1218–1224. https://doi.org/10.1126/science.abg7071.
49. Zhu, J., Mayeda, A., and Krainer, A.R. (2001). Exon identity established through differential antagonism between exonic splicing silencer-bound hnRNP A1 and enhancer-bound SR proteins. Mol. Cell *8*, 1351–1361. https://doi.org/10.1016/s1097-2765(01)00409-9.
50. Hertel, K.J. (2008). Combinatorial control of exon recognition. J. Biol. Chem. *283*, 1211–1215. https://doi.org/10.1074/jbc.R700035200.
51. Erkelenz, S., Mueller, W.F., Evans, M.S., Busch, A., Schöneweis, K., Hertel, K.J., and Schaal, H. (2013). Position-dependent splicing activation and repression by SR and hnRNP proteins rely on common mechanisms. RNA *19*, 96–102. https://doi.org/10.1261/rna.037044.112.
52. Liao, S.E., and Regev, O. (2021). Splicing at the phase-separated nuclear speckle interface: a model. Nucleic Acids Res. *49*, 636–645. https://doi.org/10.1093/nar/gkaa1209.
53. Wong, M.S., Kinney, J.B., and Krainer, A.R. (2018). Quantitative Activity Profile and Context Dependence of All Human 5′ Splice Sites. Mol. Cell *71*, 1012–1026.e3. https://doi.org/10.1016/j.molcel.2018.07.033.
54. Liao, S.E., Sudarshan, M., and Regev, O. (2023). Machine learning for discovery: deciphering RNA splicing logic. Proc. Natl. Acad. Sci. USA *120*, e2221165120. https://doi.org/10.1073/pnas.2221165120.
55. Zhang, X.H.-F., Arias, M.A., Ke, S., and Chasin, L.A. (2009). Splicing of designer exons reveals unexpected complexity in pre-mRNA splicing. RNA *15*, 367–376. https://doi.org/10.1261/rna.1498509.
56. Ray, D., Kazan, H., Chan, E.T., Peña Castillo, L., Chaudhry, S., Talukder, S., Blencowe, B.J., Morris, Q., and Hughes, T.R. (2009). Rapid and systematic analysis of the RNA recognition specificities of RNA-binding proteins. Nat. Biotechnol. *27*, 667–670. https://doi.org/10.1038/nbt.1550.
57. Scior, A., Preissler, S., Koch, M., and Deuerling, E. (2011). Directed PCR-free engineering of highly repetitive DNA sequences. BMC Biotechnol. *11*, 87. https://doi.org/10.1186/1472-6750-11-87.
58. Gossen, M., and Bujard, H. (1992). Tight control of gene expression in mammalian cells by tetracycline-responsive promoters. Proc. Natl. Acad. Sci. USA *89*, 5547–5551. https://doi.org/10.1073/pnas.89.12.5547.
59. Yeo, G., and Burge, C.B. (2004). Maximum entropy modeling of short sequence motifs with applications to RNA splicing signals. J. Comput. Biol. *11*, 377–394. https://doi.org/10.1089/1066527041410418.
60. Gaspar, I., Wippich, F., and Ephrussi, A. (2017). Enzymatic production of single-molecule FISH and RNA capture probes. RNA *23*, 1582–1591. https://doi.org/10.1261/rna.061184.117.
61. Raj, A., van den Bogaard, P., Rifkin, S.A., van Oudenaarden, A., and Tyagi, S. (2008). Imaging individual mRNA molecules using multiple singly labeled probes. Nat. Methods *5*, 877–879. https://doi.org/10.1038/nmeth.1253.
62. Schindelin, J., Arganda-Carreras, I., Frise, E., Kaynig, V., Longair, M., Pietzsch, T., Preibisch, S., Rueden, C., Saalfeld, S., Schmid, B., et al. (2012). Fiji: an open-source platform for biological-image analysis. Nat. Methods *9*, 676–682. https://doi.org/10.1038/nmeth.2019.
63. Ovesný, M., Křížek, P., Borkovec, J., Svindrych, Z., and Hagen, G.M. (2014). ThunderSTORM: a comprehensive ImageJ plug-in for PALM and STORM data analysis and super-resolution imaging. Bioinformatics *30*, 2389–2390. https://doi.org/10.1093/bioinformatics/btu202.
64. Hein, M.Y., Hubner, N.C., Poser, I., Cox, J., Nagaraj, N., Toyoda, Y., Gak, I.A., Weisswange, I., Mansfeld, J., Buchholz, F., et al. (2015). A human interactome in three quantitative dimensions organized by stoichiometries and abundances. Cell *163*, 712–723. https://doi.org/10.1016/j.cell.2015.09.053.
65. Fujioka, A., Terai, K., Itoh, R.E., Aoki, K., Nakamura, T., Kuroda, S., Nishida, E., and Matsuda, M. (2006). Dynamics of the Ras/ERK MAPK cascade as monitored by fluorescent probes. J. Biol. Chem. *281*, 8917–8926. https://doi.org/10.1074/jbc.M509344200.
66. Maharana, S., Wang, J., Papadopoulos, D.K., Richter, D., Pozniakovsky, A., Poser, I., Bickle, M., Rizk, S., Guillén-Boixet, J., Franzmann, T.M., et al. (2018). RNA buffers the phase separation behavior of prion-like RNA binding proteins. Science *360*, 918–921. https://doi.org/10.1126/science.aar7366.

STAR★METHODS

KEY RESOURCES TABLE

REAGENT or RESOURCE	SOURCE	IDENTIFIER
Antibodies		
Secondary antibody against mouse	Jackson ImmunoResearch	#715-005-150; RRID: AB_2340758
Secondary antibody against rabbit	Jackson ImmunoResearch	#711-005-152; RRID: AB_2340585
Mouse antibody against SRRM2	Sigma Aldrich	#S4045; RRID: AB_477511
Mouse antibody against SRSF1	Invitrogen	#32-4600; RRID: AB_2533080
Rabbit antibody against SON	Invitrogen	#PA5-54814; RRID: AB_2647743
Rabbit antibody against hnRNPA1	Abcam	#ab177152; RRID: AB_2925195
Chemicals, peptides, and recombinant proteins		
BsaI	New England Biolabs	#R3733
BsmBI	New England Biolabs	#R0739
BbvI	New England Biolabs	#R0173
BfuAI	New England Biolabs	#R0701
Dulbecco's Modified Eagle Medium	Gibco	#11965092
Tet system approved fetal bovine serum	Gibco	#631105
Sodium pyruvate	Thermo Fisher	#11360070
Penicillin-streptomycin	Thermo Fisher	#15070063
Lipofectamine 3000 reagent kit	Invitrogen	#L3000001
Lipofectamine RNAiMax reagent	Invitrogen	#13778075
Opti-MEM	Thermo Fisher	#31985070
Doxycycline	Santa Cruz	# sc-204734B
Pladienolide B	Cayman Chemicals	#445493-23-2
Triptolide	Sigma Aldrich	#T3652-1MG
Phusion® High-Fidelity DNA Polymerase	New England Biolabs	#M0530L
Lipofectamine RNAiMax reagent	Invitrogen	#13778150
Amino-11-ddUTP	Lumiprobe	#15040
Terminal transferase	New England Biolabs	#M0315L
Alexa Fluor 647 succinimidyl ester	Invitrogen	#A20106
CF568 succinimidyl ester	Sigma Aldrich	#SCJ4600027
Alexa Fluor 750 succinimidyl ester	Invitrogen	#A20011
Alexa Fluor 488 succinimidyl ester	Invitrogen	# A20000
Paraformaldehyde	Electron Microscopy Sciences	#15710
Triton X-100	Thermo Fisher	#BP151-100
Vanadyl ribonucleoside complexes	Sigma-Aldrich	#R3380
Formamide	Ambion	#AM9342
Dextran sulphate	Sigma-Aldrich	#D8906
Dithiothreitol	Sigma-Aldrich	#10197777001
Ultrapure BSA	Invitrogen	#AM2618
Glucose oxidase	Sigma-Aldrich	#G2133
Catalase	Sigma-Aldrich	#C3515
β-mercaptoethanol	Sigma-Aldrich	#M3148
Critical commercial assays		
RNA extraction kit	QIAgen	#74104

(*Continued on next page*)

Continued

REAGENT or RESOURCE	SOURCE	IDENTIFIER
RNA extraction kit	QIAgen	#75144
TURBO DNA-*free*™ kit	Thermofisher	#AM1907
Reverse Transcription SuperScript IV	Thermofisher	#18090010
iScript cDNA synthesis kit	BioRad	#1708890
Deposited data		
Code used for radial distribution analysis and toy model development	This paper	(https://github.com/JingyiFeiLab/Radial-distribution_Toy-model)
Experimental models: Cell lines		
HeLa Tet-On cells	TaKaRa Bio, USA	#631183
Oligonucleotides		
SRSF1 siRNA	Integrated DNA Technologies, USA	hs.Ri.SRSF1.13.2
hnRNPA1 siRNA	Integrated DNA Technologies, USA	hs.Ri.HNRNPA1.13.2
Scrambled double-stranded siRNA	Integrated DNA Technologies, USA	DsiRNA
RNA FISH probes	Integrated DNA Technologies, USA	Table S2
Primers	Integrated DNA Technologies, USA	Table S2
Construction oligomers	Integrated DNA Technologies, USA	Table S2
Recombinant DNA		
Plasmids: $WT_{S1\text{-}H1}$, $WT_{S7\text{-}H1}$, $MUT_{S1\text{-}H1}$, $MUT_{S1\text{-}H1,NR}$, $MUT_{S7\text{-}H1}$, $MUT_{N\text{-}H1}$, $MUT_{S1\text{-}N}$, $MUT_{S1\text{-}spacer\text{-}H1}$, $WT_{H1\text{-}S1}$	This paper	Addgene (218392-218400)
Software and algorithms		
Stellaris Probe Designer	LGC Biosearch Technologies	https://www.biosearchtech.com/support/tools/design-software/stellaris-probe-designer
Fiji (ImageJ)	Schindelin et al.[53]	https://imagej.nih.gov/ij/
NIS-Elements	Nikon	https://www.microscope.healthcare.nikon.com/products/software/nis-elements
Thunderstorm ImageJ plugin	Ovesný et al.[54]	https://zitmen.github.io/thunderstorm/
MATLAB	MathWorks	https://www.mathworks.com/products/matlab.html
Wolfram Mathematica	Wolfram	https://www.wolfram.com/mathematica/
OriginPro	OriginLab	https://www.originlab.com/index.aspx?go=downloads
BLAST	National Library of Medicine	https://blast.ncbi.nlm.nih.gov/Blast.cgi
Snapgene v7.0.1	Dotmatics	https://www.snapgene.com/
Other		
Imaging chamber, #1.5 cover glass	Cellvis	#C8-1.5H-N
P-6 Micro Bio-Spin Column	Bio-Rad	#7326222
TetraSpeck microspheres	Invitrogen	#T7279

RESOURCE AVAILABILITY

Lead contact

Further information and requests for resources and reagents should be directed to and will be fulfilled by the lead contact, JF (jingyifei@uchicago.edu).

Materials availability

All plasmids used in this study are available through the lead contact and through AddGene (218392-218400).

Data and code availability

- Data: The authors declare that all data supporting the findings of the present study are available in the article and its supplemental figures and tables.
- Code: Code used for radial distribution analysis and toy model development is available on GitHub (https://github.com/JingyiFeiLab/Radial-distribution_Toy-model).
- Any additional information will be made available upon request from the lead contact.

EXPERIMENTAL MODEL AND STUDY PARTICIPANT DETAILS

Cell lines

HeLa Tet-On 3G cell lines were obtained from TaKaRa Bio. Cell lines tested negative for mycoplasma contamination.

METHOD DETAILS

Plasmid design and construction

Plasmid design was based on our earlier work.[32,55] Briefly, a three-exon construct was used, consisting of a Tet-responsive promoter, Chinese hamster *DHFR* exon 1 and intron 1, a synthetic variable region around exon 2, an intronic sequence derived from *DHFR* intron 3 (with a mutation in the 3′ splice site for the MUT family of constructs), and finally, the concatenation of *DHFR* exons 4 through 6 followed by the SV40 polyA sequence in the strong orientation. The SR motif-rich region in exon 2 consists of 15 repeats of an 8nt SR-binding sequence (either SRSF1 or SRSF7) separated by an 8nt "neutral" reference sequence (in total 248 nt), and is flanked by 3′ and 5′ splice sites. An hnRNPA1 motif-rich region with 24 repeats was designed similarly (392 nt), with the 8nt hnRNPA1 binding sequence chosen for affinity and specificity based on RNAcompete data.[56] This region was placed downstream of exon 2 (except in $WT_{H1\text{-}S1}$, where it was placed upstream). The neutral sequences in $MUT_{S1\text{-}spacer\text{-}H1}$, $MUT_{S1\text{-}N}$, and $MUT_{N\text{-}H1}$ were derived from repeats of the reference sequence, and were of 720 nt as the spacer in $MUT_{S1\text{-}spacer\text{-}H1}$ and size-matched as intron (392 nt) or exon (238 nt) sequences in the other two cases.

Constructs $MUT_{S1\text{-}H1}$, $MUT_{S1\text{-}spacer\text{-}H1}$, $WT_{S1\text{-}H1}$, $WT_{H1\text{-}S1}$, $MUT_{S1\text{-}N}$, $MUT_{N\text{-}H1}$, $WT_{S7\text{-}H1}$, and $MUT_{S7\text{-}H1}$ were generated in three steps. In the first step, SR motif-rich region, neutral reference sequence, and hnRNPA1 motif-rich region were generated separately to produce intermediate plasmids,[32] following a previously published PCR-free cloning approach.[57] Briefly, type IIS enzymes (BsaI, New England Biolabs #R3733, and BsmBI, New England Biolabs #R0739) were used to iteratively concatenate sequence modules. In the second step, the intermediate plasmids were combined with a plasmid containing the 5′ splice site or the 3′ splice site using the same stepwise approach. For example, for plasmid $WT_{S1\text{-}H1}$, an intermediate plasmid was obtained containing the SR motif-rich region followed by a 5′ splice site and then the hnRNP motif-rich region. In the third step, the assembled sequences were transferred to the appropriate target plasmids (WT, MUT) by using a different set of type IIS enzymes (BbvI, New England Biolabs #R0173, and BfuAI, New England Biolabs #R0701). Importantly, these plasmids contain a tetracycline responsive promoter.[32,58]

The non-repeat construct $MUT_{S1\text{-}H1,NR}$ was obtained from $MUT_{S1\text{-}H1}$ by mutating each nucleotide in the SR and hnRNP motif-rich regions with a probability of 37.5%. Doing so is likely to introduce unwanted splice site sequences, and to abolish certain RBP binding motifs. We therefore ranked *in silico* 10,000 candidate sequences for each region (SR rich and hnRNP rich) and picked sequences that (1) contain no predicted splice site sequence,[53,59] and (2) keep a similar enrichment of SR or hnRNP motifs as scored using our previous machine learning model.[54] The final sequences contained over 30% mutations compared to the original ones. Using BLAST of the sequence against itself, we verified the absence of any residual repeats. Gene fragments were then synthesized using gBlocks™ (IDT) and cloned into the same target plasmids.

All plasmids were verified using whole-plasmid sequencing (Plasmidsaurus). Sequence information can be found in Data S2 and through Addgene (218392-218400).

Cell culture, transfection, and drug treatments

HeLa Tet-On cells (TaKaRa) were cultured in high glucose (4.5 g/L) containing Dulbecco's Modified Eagle Medium (DMEM, Gibco) supplemented with 10% fetal bovine serum (FBS, Gibco), 1 mM sodium pyruvate (Gibco), 50 U/mL penicillin-streptomycin (Gibco). Cells were grown at 37°C in a humidified environment containing 5% CO_2. For imaging, cells were seeded in an eight-well imaging chamber (#1.5 cover glass, Cellvis) and grown overnight to 70–80% confluency before transfection.

For transfecting each well, 0.6 μL of Lipofectamine 3000 reagent (Invitrogen) was diluted in pre-warmed 15 μL reduced serum minimum essential medium (opti-MEM, Gibco) and vortexed briefly. In another tube, 200 ng of plasmid DNA and 0.4 μL P3000 reagent (Invitrogen) were diluted in 15 μL pre warmed opti-MEM and vortexed briefly. The two solutions were mixed, vortexed briefly and incubated for 15 min at room temperature. The cell culture medium was replaced with pre-warmed DMEM containing 10% Tet system approved FBS (Tet-free medium, TaKaRa) and 30 μL of DNA-lipid complex was added to each well. The medium was replaced with fresh Tet-free medium 6–8 h after transfection and incubated overnight.

30 min or 2 h transcription induction of the transfected construct was done 24 h after transfection using 2 μg/mL doxycycline (Santa Cruz # sc-204734B) in Tet-free medium. For samples where splicing inhibition was required, cells were treated with 100 nM Pladienolide B (Plad B,

Cayman) in Tet-free medium for 4 h. For transcription inhibition, induction with doxycycline was done for 2 h followed by treatment with Triptolide (40 μM, Sigma Aldrich) for 1 h.

RT-PCR for biochemical assays

RNA was extracted 20 h after transfection using QIAgen RNeasy minikits (#74104) in a QIAcube following the manufacturer's protocol. DNA was removed using TURBO DNase (Thermofisher #AM2238) in a 30 μL reaction. RNA was then quantified using a Nano Drop One (Thermofisher #ND-ONE-W), and the concentration was adjusted to 60 ng/uL. For reverse transcription, 200 ng of RNA were used for a 10 μL reaction using SuperScript IV (Thermofisher #18090010) according to the manufacturer's protocol. Appropriate RT primers (Table S2) were added at a final concentration of 100 nM. PCR reactions were carried out in a Veriti 96-well thermocycler (Applied Biosystems #4375305) using a Phusion High Fidelity kit (New England Biolabs #E0553L). The reverse transcription product was diluted 5-fold with water and 2 μL was used in a 25 μL PCR reaction according to the manufacturer's instructions. PCR was run for 21 or 22 cycles allowing 2 min for extension. The PCR product was run in 1.5% agarose gels and quantified in a BioRad gel documentation system after post-staining with Ethidium Bromide and destaining.

siRNA-mediated knockdown

SRSF1 and hnRNPA1 knockdown was performed using double-stranded siRNAs against SRSF1 (hs.Ri.SRSF1.13.2, IDT, USA) and hnRNPA1 (hs.Ri.HNRNPA1.13.2, IDT, USA). A scrambled double-stranded siRNA (DsiRNA, IDT, USA) was used as negative control. Cells were seeded in an eight-well imaging chamber and grown to 60–70% confluency. For each well, 1.5 μL Lipofectamine RNAiMax reagent (Invitrogen) was diluted in 25 μL pre-warmed opti-MEM and vortexed briefly. In a separate tube, 0.5 μL siRNA (10 μM) was diluted in 25 μL pre-warmed opti-MEM and vortexed. The two solutions were then mixed, vortexed and incubated at room temperature for 5 min. 25 μL was then added to each well after replacing the cell culture medium with Tet-free medium. 6–8 h after transfection, fresh Tet-free medium was added. For the experiments with constructs, siRNA knockdown was done using Lipofectamine RNAiMax reagent followed by plasmid transfection using Lipofectamine 3000 with an interval of 24 h.

qPCR quantification for knockdown efficiency

HeLa Tet-On cells were grown in a 12-well plate and siRNA mediated knockdown was performed. RNA extraction was done using the Qiagen RNeasy kit (Qiagen, #75144) following the provided protocol. cDNA was synthesized using an iScript cDNA synthesis kit (BioRad). 0.5–1 μg RNA template was used and the reaction was performed in a thermal cycler (Applied Biosystems) as follows: priming for 5 min at 25°C, reverse transcription (RT) for 20 min at 46°C, RT inactivation for 1 min at 95°C and then held at 4°C. For qPCR, 2 μL of cDNA was mixed with 2 μL of forward and reverse primers (2.5 μM each, Table S2) and 1x SYBR Green Supermix (BioRad) for a final reaction volume of 20 μL. The qPCR reactions were performed using the CFX real-time PCR system (Bio-Rad) as follows: pre-incubation of 95°C for 30 s, followed by 40 cycles consisting of 95°C for 10 s and 60°C for 30 s. The reactions were then subjected to melting curve analysis: 95°C for 10 s, 65°C for 5 s followed by 0.5°C increments to 95°C for 5 s. The data was analyzed with the BioRad CFX Maestro software.

Labeling of FISH probes and secondary antibodies

FISH probes were designed using the Stellaris Probe Designer with masking level set to 5 to avoid non-specific binding and purchased from IDT. Probes were 18–20 nucleotides long with a GC content between 45% and 55%. The probes targeting motifs with SRSF1, SRSF7 and hnRNPA1 in $WT_{S1\text{-}H1}$, $MUT_{S1\text{-}H1}$, $WT_{H1\text{-}S1}$, $WT_{S7\text{-}H1}$, $MUT_{S7\text{-}H1}$, $MUT_{S1\text{-}N}$, and $MUT_{N\text{-}H1}$ were purchased with 3′ amine modification. For the other probes, amine modification was added using terminal transferase (TdT) enzymatic reaction.[60] For a 60 μL reaction volume, 40 μL of pooled oligonucleotides (100 μM) were mixed with 12 μL Amino-11-ddUTP (1 mM, Lumiprobe), 2.4 μL TdT (20000 U/mL, New England Biolabs, #M0315L) in 1x TdT buffer (New England Biolabs) and incubated overnight at 37°C in a PCR thermocycler (Applied Biosystems). The modified probes were purified using a P-6 Micro Bio-Spin Column (Bio-Rad).

For fluorophore conjugation, amine modified probes were dissolved in 0.1 M sodium bicarbonate (pH 8.5). Alexa Fluor (Invitrogen) and CF568 (Sigma Aldrich)-conjugated succinimidyl ester were dissolved in 0.5–4 μL DMSO and mixed with the probe solution. The dye: probe molar ratio was 25:1 approximately. The labeling reaction was incubated overnight in dark at 37°C. To quench the reaction, $1/9^{th}$ reaction volume of 3M sodium acetate (pH 5) was added. Labeled probes were precipitated overnight with ethanol (~2.5-fold of the reaction volume) and then passed through a P-6 Micro Bio-Spin column to remove unconjugated free dye. The labeling efficiency of all probes was above 75%. The exact sequences of the FISH probes are provided in Table S2.

Secondary antibodies against mouse (Jackson ImmunoResearch, #715-005-150) or rabbit (Jackson ImmunoResearch, #711-005-152) were labeled with Alexa Fluor succinimidyl ester. 24 μL antibody (1 mg/mL) was mixed with 3 μL 10x PBS and 3 μL sodium bicarbonate (1 M, pH 8.5). 0.001–0.003 mg of Alexa dye was added to the above solution and the reaction was incubated for 1 h at room temperature. Labeled antibodies were purified using a P-6 Micro Bio-Spin column equilibrated with 1x PBS. 0.8 to 2.2 dye per antibody was typically achieved.

RNA FISH and immunostaining

RNA FISH and immunostaining were performed according to a previously published protocol.[61] Cells were fixed with 4% paraformaldehyde (PFA, Electron Microscopy Sciences) in 1x PBS for 10 min at room temperature. Permeabilization was done with a solution containing 0.5% Triton X-100 (Thermo Scientific) and 2 mM vanadyl ribonucleoside complexes (Sigma-Aldrich, #R3380) in 1x PBS for 10 min on ice. Cells were

washed 3 times with 1x PBS for at least 5 min after fixation and permeabilization. Cells were stored in 70% ethanol at 4°C until hybridization with FISH probes. Cells were washed with 2x saline sodium citrate (SSC) two times followed by a final wash with FISH wash solution (10% formamide (Ambion, #AM9342) in 2x SSC). 125 μL of hybridization buffer (FISH wash solution and 10% dextran sulfate (Sigma-Aldrich)) containing 5 nM of each labeled probe and 10 mM dithiothreitol (Sigma-Aldrich) was added to each well of the imaging chamber. The hybridization reaction was incubated overnight at 37°C in the dark. The following day, cells were washed with FISH wash solution for 30 min at 37°C.

To prevent dissociation of probes during immunostaining, cells were again fixed with 4% PFA for 10 min at room temperature. After washing with 1x PBS, cells were treated with blocking solution (0.1% ultrapure BSA (Invitrogen, #AM2618) in 1x PBS) for 30 min at room temperature. Solutions of primary antibodies were prepared in blocking solution using the following dilutions: mouse antibody against SRRM2 (1:2000, Sigma Aldrich, #S4045), mouse antibody against SRSF1 (1:250, Invitrogen, #32–4600), rabbit antibody against hnRNPA1 (1:100, Abcam, #ab177152), rabbit antibody against SON (1:200, Invitrogen, #PA5-54814). 125 μL of the solution was added to each well and incubated at room temperature for 1 h. Cells were washed with 1x PBS three times with 5 min incubation each time. Labeled secondary antibodies were diluted 200-fold in blocking solution, with 125 μL added to each well and incubated for 1 h at room temperature. Cells were washed with 1x PBS for 3 times with at least 5 min incubation time and stored in 4x SSC at 4°C until imaging.

Imaging and image reconstruction

Diffraction limited epi imaging was performed using a Nikon TiE microscope with a CFI HP TIRF objective (100X, NA 1.49, Nikon), and an EMCCD (Andor, iXon Ultra 888). Imaging was performed using an imaging buffer containing Tris-HCl (50 mM, pH 8), 10% glucose, 2x SSC, glucose oxidase (0.5 mg/mL, Sigma-Aldrich) and catalase (67 μg/mL, Sigma-Aldrich). FISH signals on the RNAs were imaged using the 647 nm laser (Cobolt MLD) and 561 nm laser (Coherent Obis). The immunofluorescence signal on nuclear speckle marker proteins was imaged using a 488 nm laser (Cobolt MLD). For the knockdown experiments, a 750 nm laser (Shanghai Dream Lasers Technology) was used to look at SRSF1 or hnRNPA1 protein levels stained with Alexa Fluor 750. Images were then processed in Fiji (ImageJ)[62] for further analysis.

2D-SMLM was performed with the same microscope, objective and EMCCD. Fluorescent TetraSpeck beads (0.1 μm, Invitrogen) were diluted 500-fold in 1x PBS, added to each well and incubated for 15 min at room temperature. After washing with 1x PBS to remove unattached beads, the same imaging buffer (as above) with additional 100 mM β-mercaptoethanol (BME, 14.3 M, Sigma-Aldrich) was added to the imaging chamber. For two color STORM, movies were collected for the AF647 and CF568 channels sequentially using JOBS module in the NIS software. Briefly, the 647 nm (~40 mW) and 561 nm laser (~85 mW) were used to excite AF647 and CF568 fluorophore, respectively. A 405 nm laser (CL2000, Crystal Laser) was used for activation of fluorophores from 'off' to 'on' state. The acquisition was performed with 3 frames of 647 or 561 nm laser excitation followed by 1 frame of 405 nm laser excitation, using an exposure time of 42 ms. The 405 nm laser power was adjusted during the acquisition to maintain a reasonable density of fluorophores in the 'on-state'. The maximum 405 nm laser power used with 647 and 561 lasers was ~2.2 mW and ~4 mW, respectively. A total of 15000 frames were recorded for each 647 and 561 channels. Before performing SMLM imaging on a selected cell, an epi image of the same cell with at least one bead present in the region of interest was taken for channel alignment.

SMLM image reconstruction was performed using the Thunderstorm[63] ImageJ plugin. For approximate localization of molecules, 'local maximum' method was used with the peak intensity threshold 2 times the standard deviation of the residual background. To determine sub-pixel localization of molecules, the Point Spread Function (Integrated Gaussian) method was used with fitting radius of 3 pixels (pixel size = 130 nm) and initial sigma as 1.6 pixels. The 'connectivity' was set to '8-neighborhood'. The images were then corrected for translational drift using the cross-correlation method and a bin size of 20–25. Finally, spots with xy-uncertainty more than 45 nm were filtered out. Images were then rendered with 5x magnification and lateral shifts 5.

Data analysis

A custom MATLAB code that we previously developed[16] was modified for radial distribution analysis on reconstructed SMLM images. Briefly, grayscale images were created from the mean intensity of all three fluorescence channels. Nuclear speckles were identified by applying an appropriate intensity threshold on the grayscale image. Inappropriately fragmented nuclear speckles were removed from the final analysis by applying a size cutoff. Further processing was done on the 2D binary images by filling and opening binary operations to remove internal voids and shot noise. Each identified nuclear speckle was indexed in region of interest (ROI), and the geometric centroid of the mask served as the center of each speckle. Additional thresholds on 2D-area and ellipticity were applied to discard abnormally large (fused) nuclear speckles and speckles that largely deviated from a spherical shape, respectively. Ellipticity was calculated as $\sqrt{((a^2 - c^2)/a^2)}$, where a is the equatorial radius and c is the polar radius assuming an elliptical fit to the nuclear speckles. An area cut-off of 5000 pixels (at pixel size of 26 nm) and ellipticity cut-off of 0.8 worked best for our analysis. To estimate the 'regularity' of the surface of the nuclear speckles, the number of edge pixels were counted using the MATLAB built-in function *bwperim* on the generated intensity mask of the speckle and divided by the area of the speckle. For calculating the distance of the RNA motifs to the center of the nuclear speckle, the normalized radial distribution of intensity of each channel was calculated from the defined center of the speckle. The mean distance of AF647 and CF568 signals (reporting the RNA signals) was calculated for each nuclear speckle, normalized by the size of the speckle (intensity weighted average radius of SRRM2/SON signal), and represented as scatterplots. For calculating the distance of the RNA motifs to the edge of the nuclear speckle, MATLAB built-in function *bwboundaries* was used to trace the exterior boundaries of nuclear speckles. For each pixel, distance to the edge is defined

as the distance between that pixel and the nearest pixel on the boundary. The same procedures as described above were performed to obtain the normalized radial distribution functions and scatterplots with respect to the edge of speckles.

Modeling details

We employed a toy model, in which we considered the space as four lattice sites with two in the nuclear speckle and two in the nucleoplasm. The RNA molecule was modeled as adjacent SRSF1 and hnRNPA1 motifs, which were allowed to occupy two adjacent lattice sites. As a result, there were 6 possible configurations of RNA positions and orientations. Furthermore, each configuration can be found in one of four binding states corresponding to SRSF1 and hnRNPA1 protein being either bound or unbound (Figure 7A). We denote the occupancy of SRSF1 and hnRNPA1 as σ_s and σ_h respectively, taking value 0 (unbound) or 1 (bound). A detailed summary of the 24 states, considering all the possible RNA spatial configurations as well as protein binding, can be found in Table S1.

The energy for the i th state can be written as

$$E^i = \sigma_s^i \varepsilon_s^i + \sigma_h^i \varepsilon_h^i.$$

ε is a measure of RNA-RBP interaction and is given by

$$\varepsilon = -\frac{1}{\beta} ln\left(\frac{c}{K_d}\right)$$

where c is the RBP concentration in each compartment and K_d is the dissociation constant of the RBP to its RNA motif. Here ε is not the usual RNA-RBP binding affinity defined by $\frac{1}{\beta} ln\left(\frac{K_d}{1\ M}\right)$, but an effective energy to account for the concentration dependence of binding probability. With this definition of ε, the probability of the protein bound state follows a Boltzmann distribution

$$p_b = \frac{c/K_d}{1+c/K_d} = \frac{e^{-\beta\varepsilon}}{1+e^{-\beta\varepsilon}}.$$

The effective energy between SRSF1 and its binding motif (ε_s^i), and the effective energy between hnRNPA1 and its binding motif (ε_h^i) depend on SRSF1 and hnRNPA1 motif position, and are given by

$$\varepsilon_s^i = \begin{cases} \varepsilon_{s1} = -\frac{1}{\beta} ln\left(\frac{c_{s1}}{K_d}\right), x_s^i \leq 2 \\ \varepsilon_{s2} = -\frac{1}{\beta} ln\left(\frac{c_{s2}}{K_d}\right), \ x_s^i > 2 \end{cases}$$

$$\varepsilon_h^i = \begin{cases} \varepsilon_{h1} = -\frac{1}{\beta} ln\left(\frac{c_{h1}}{K_d}\right), x_h^i \leq 2 \\ \varepsilon_{h2} = -\frac{1}{\beta} ln\left(\frac{c_{h2}}{K_d}\right), \ x_h^i > 2 \end{cases}$$

where ε_{s1} and ε_{s2} denote the effective energy between SRSF1 and its binding motif in nuclear speckles and nucleoplasm, c_{s1} and c_{s2} denote nuclear speckle and nucleoplasmic concentration of SRSF1, ε_{h1} and ε_{h2} denote the effective energy between hnRNPA1 and its binding motif in nuclear speckles and nucleoplasm, c_{h1} and c_{h2} denote nuclear speckle and nucleoplasmic concentration of hnRNPA1, x_s^i and x_h^i denote SRSF1 and hnRNPA1 motif position for the i th state taking values in $\{1,2,3,4\}$.

To determine values for ε_{s1} and ε_{s2}, we first estimated SRSF1 concentration in nuclear speckles (c_{s1}) and nucleoplasm (c_{s2}). They are given by $c_{s1} = N_1/V_1$ and $c_{s2} = N_2/V_2$, where N_1 and N_2 denote the number of molecules in nuclear speckles and nucleoplasm, V_1 and V_2 denote the volume of nuclear speckles and nucleoplasm. The copy number of SRSF1 proteins in HeLa cells was measured earlier as 4.4×10^6 molecules per cells by mass spectrometry.[64] Because SRSF1 proteins predominantly localize to nucleus, we used this number as the number of molecules in nucleus. By immunofluorescence images, we found 17.4% of SRSF1 signals present in nuclear speckles and 82.6% present in nucleoplasm. N_1 and N_2 were therefore estimated to be 7.7×10^5 and 3.6×10^6. The average volume of HeLa cell nucleus was reported to be 220 fL.[65] Using our imaging data, we estimated that 14.0% of nuclear space was occupied by nuclear speckles. We therefore calculated V_1 and V_2 to be 30.8 fL and 189.2 fL. c_{s1} and c_{s2} were then estimated to be 41.0 μM and 31.7 μM, respectively. ε_{s1} and ε_{s2} were determined by assuming K_d to be 1 μM.

The nucleoplasmic concentration of hnRNPA1 protein c_{h2} was estimated as 36.4 μM based on reported values.[66] To estimate the nuclear speckle concentration of hnRNPA1 c_{h1}, we analyzed the depletion of hnRNPA1 intensity in immunofluorescence images. We found 55% of nuclear speckles exhibited 30% depletion in hnRNPA1, 30% exhibited 6% depletion, and 15% exhibited no depletion. Based on this, we generated three separate simulations recapitulating various degrees of depletion in hnRNPA1 and computed the population average. Again, we used K_d as 1 μM to determine ε_{h1} and ε_{h2}.

When simulating knockdown experiments, the protein concentrations were multiplied by $1-x$, where x represents the knockdown efficiency, ε_{s1}, ε_{s2}, ε_{h1}, and ε_{h2} vary accordingly as concentrations decrease.

Given the energy E^i, we can find the partition function and the probability for the i th state by the Boltzmann distribution

$$Z = \sum_{i=1}^{24} e^{-\beta E_i}, P^i = \frac{e^{-\beta E_i}}{Z}.$$

The probability distribution of SRSF1 motif position $P(x_s = j)$ and hnRNPA1 motif position $P(x_h = j)$ are given by the sum of the probabilities for states with SRSF1 motif position equal to j and hnRNPA1 motif position equal to j respectively. Then the mean position of SRSF1 and hnRNPA1 are determined by

$$\overline{x_s} = \sum_{j=1}^{4} jP(x_s = j), \overline{x_h} = \sum_{j=1}^{4} jP(x_h = j).$$

All analytical expressions for the partition function and the mean position of SRSF1 and hnRNPA1 motif were obtained by Wolfram Mathematica as

$$Z = e^{-\beta\varepsilon_{h1}}\left(3 + 2e^{-\beta\varepsilon_{s1}} + e^{-\beta\varepsilon_{s2}}\right) + e^{-\beta\varepsilon_{h2}}\left(3 + e^{-\beta\varepsilon_{s1}} + 2e^{-\beta\varepsilon_{s2}}\right) + 6 + 3e^{-\beta\varepsilon_{s1}} + 3e^{-\beta\varepsilon_{s2}}$$

$$\overline{x_s} = \frac{e^{-\beta\varepsilon_{h1}}\left(6+3e^{-\beta\varepsilon_{s1}}+3e^{-\beta\varepsilon_{s2}}\right)+e^{-\beta\varepsilon_{h2}}\left(9+2e^{-\beta\varepsilon_{s1}}+7e^{-\beta\varepsilon_{s2}}\right)+15+5e^{-\beta\varepsilon_{s1}}+10e^{-\beta\varepsilon_{s2}}}{Z}$$

$$\overline{x_h} = \frac{e^{-\beta\varepsilon_{h1}}\left(5+3e^{-\beta\varepsilon_{s1}}+2e^{-\beta\varepsilon_{s2}}\right)+e^{-\beta\varepsilon_{h2}}\left(10+3e^{-\beta\varepsilon_{s1}}+7e^{-\beta\varepsilon_{s2}}\right)+15+6e^{-\beta\varepsilon_{s1}}+9e^{-\beta\varepsilon_{s2}}}{Z}$$

$$\overline{x_h} - \overline{x_s} = \frac{e^{-\beta\varepsilon_{h2}}\left(1+e^{-\beta\varepsilon_{s1}}\right) - e^{-\beta\varepsilon_{h1}}\left(1+e^{-\beta\varepsilon_{s2}}\right)+e^{-\beta\varepsilon_{s1}} - e^{-\beta\varepsilon_{s2}}}{Z}$$

These expressions indicate that this model can account for the differential intra-speckle spatial distribution of SRSF1 and hnRNPA1 motif, which is driven by the enrichment of SRSF1 and depletion of hnRNPA1 in nuclear speckles (Figure 7B). In agreement with our observations, this model predicts that both SRSF1 and hnRNPA1 motifs migrate toward the speckle periphery upon SRSF1 knockdown and toward the speckle interior upon hnRNPA1 knockdown (Figures 7C and 7D). Moreover, the difference in spatial distribution of SRSF1 and hnRNPA1 motif is maintained under knockdown conditions, consistent with our experimental observations (Figures 7C and 7D).

We finally tested this model applies to a broad range of binding affinities by increasing K_d to 10 μM and decreasing K_d to 100 nM. Similar trends were found in Figure S13.

QUANTIFICATION AND STATISTICAL ANALYSIS

Data points in the intensity vs. distance plots represent mean ± standard deviation from two-three biological replicates. Scatterplots are generated by combining all nuclear speckles from two-three biological replicates and the values represent mean ± standard error of mean (s.e.m.). p values in the scatterplots are calculated with paired sample Wilcoxon signed rank test (one-sided) and two sample t-test (one-sided), with $*p < 5e\text{-}2$, $**p < 1e\text{-}2$, $***p < 1e\text{-}3$ and $p < 5e\text{-}2$ is considered statistically significant. Replicates are biological replicates collected from different dishes of cells and measured on different days. Statistical details along with the number of nuclear speckles/cells analyzed for each experiment are mentioned in the figure captions. MATLAB was used to analyze the raw imaging data and the plots and statistical significance tests were done in OriginPro.